2015-06

The design and construction of a long-distance atmospheric propagation test chamber

Torrealba, Roberto A.

Monterey, California: Naval Postgraduate School

NAVAL POSTGRADUATE SCHOOL

MONTEREY, CALIFORNIA

THESIS

THE DESIGN AND CONSTRUCTION OF A LONG-DISTANCE ATMOSPHERIC PROPAGATION TEST CHAMBER

by

Roberto A. Torrealba

June 2015

Thesis Advisor: Keith R. Cohn
Second Reader: Joseph Blau

Approved for public release; distribution is unlimited

THIS PAGE INTENTIONALLY LEFT BLANK

REPORT DOCUMENTATION PAGE

Form Approved OMB No. 0704–0188

1. AGENCY USE ONLY *(Leave blank)*	**2. REPORT DATE** June 2015	**3. REPORT TYPE AND DATES COVERED** Master's Thesis

4. TITLE AND SUBTITLE
THE DESIGN AND CONSTRUCTION OF A LONG-DISTANCE ATMOSPHERIC PROPAGATION TEST CHAMBER

5. FUNDING NUMBERS

6. AUTHOR(S) Roberto A. Torrealba

7. PERFORMING ORGANIZATION NAME(S) AND ADDRESS(ES)
Naval Postgraduate School
Monterey, CA 93943-5000

8. PERFORMING ORGANIZATION REPORT NUMBER

9. SPONSORING /MONITORING AGENCY NAME(S) AND ADDRESS(ES)
N/A

10. SPONSORING/MONITORING AGENCY REPORT NUMBER

11. SUPPLEMENTARY NOTES The views expressed in this thesis are those of the author and do not reflect the official policy or position of the Department of Defense or the U.S. Government. IRB Protocol number ____N/A____.

12a. DISTRIBUTION / AVAILABILITY STATEMENT	**12b. DISTRIBUTION CODE**
Approved for public release; distribution is unlimited	A

13. ABSTRACT (maximum 200 words)

The experiment for this thesis first involved using a laser modeling tool called ANCHOR to compare two 100kW lasers in a potential operational theater, one with a wavelength of 1.0642 μm, and the other with a wavelength of 1.5314 μm. This modeling illustrated that the laser's effective range can be greatly reduced due to haze or humidity (or both), depending on its lasing wavelength.

The second part of this thesis describes a multi-pass spectroscopic experimental setup that employs a White cell, which can be used to measure atmospheric extinction coefficients in a controlled manner. The first results from this setup produced consistent, comparable atmospheric extinction values.

14. SUBJECT TERMS Directed energy weapons, high energy lasers, atmospheric propagation, White cell chambers	**15. NUMBER OF PAGES** 83
	16. PRICE CODE

17. SECURITY CLASSIFICATION OF REPORT	**18. SECURITY CLASSIFICATION OF THIS PAGE**	**19. SECURITY CLASSIFICATION OF ABSTRACT**	**20. LIMITATION OF ABSTRACT**
Unclassified	Unclassified	Unclassified	UU

NSN 7540–01-280-5500

Standard Form 298 (Rev. 2–89)
Prescribed by ANSI Std. 239–18

THIS PAGE INTENTIONALLY LEFT BLANK

Approved for public release; distribution is unlimited

THE DESIGN AND CONSTRUCTION OF A LONG-DISTANCE ATMOSPHERIC PROPAGATION TEST CHAMBER

Roberto A. Torrealba
Ensign, United States Navy
B.S., United States Naval Academy, 2014

Submitted in partial fulfillment of the
requirements for the degree of

MASTER OF SCIENCE IN APPLIED PHYSICS

from the

NAVAL POSTGRADUATE SCHOOL
June 2015

Author: Roberto A. Torrealba

Approved by: Keith R. Cohn
Thesis Advisor

Joseph Blau
Second Reader

Andres Larraza
Chair, Department of Physics

THIS PAGE INTENTIONALLY LEFT BLANK

ABSTRACT

The experiment for this thesis first involved using a laser modeling tool called ANCHOR to compare two 100kW lasers in a potential operational theater, one with a wavelength of 1.0642 μm, and the other with a wavelength of 1.5314 μm. This modeling illustrated that the laser's effective range can be greatly reduced due to haze or humidity (or both), depending on its lasing wavelength.

The second part of this thesis describes a multi-pass spectroscopic experimental setup that employs a White cell, which can be used to measure atmospheric extinction coefficients in a controlled manner. The first results from this setup produced consistent, comparable atmospheric extinction values.

THIS PAGE INTENTIONALLY LEFT BLANK

TABLE OF CONTENTS

LIST OF FIGURES

THIS PAGE INTENTIONALLY LEFT BLANK

LIST OF TABLES

THIS PAGE INTENTIONALLY LEFT BLANK

LIST OF ACRONYMS AND ABBREVIATIONS

AFIT	Air Force Institute of Technology
ANCHOR	atmospheric NPS code for high-energy laser optical propagation
CIWS	close-in weapon system
DE	directed energy
ERL	energy recovery linac
FEL	free-electron laser
FTIR	Fourier Transform infrared
HEL	high-energy laser
HeNe	helium-neon
HITRAN	high-resolution transmission molecular absorption database
HMMWV	high mobility multi-purpose wheeled vehicle
LaWS	laser weapon system
LCS	littoral combat ship
LEEDR	laser environmental effects definition and reference
LINAC	linear accelerator
RAM	rolling airframe missile
SSL	solid state laser
USAF	United States Air Force
USN	Unites States Navy
USS	United States ship
WC	White cell

THIS PAGE INTENTIONALLY LEFT BLANK

ACKNOWLEDGEMENTS

First and foremost, I would like to sincerely thank Professor Keith Cohn for his daily guidance, extreme patience, and personal commitment to the completion of this thesis. I would also like to recognize Professors Joseph Blau, Bill Colson, Gamani Karunasiri, Fabio Alves, and the rest of the NPS faculty for their boundless knowledge and staggering support. Without their help, not only would I not have been able to accomplish this endeavor, I would also not have learned the vast amount that I have learned in the past eleven months. Additionally, thank you to Dick Lind from the NPS meteorology department for loaning us the hygrometer used to in this project.

Secondly, I would like to thank my family for their unconditional love and encouragement. Without their constant advice, foresight, and countless sacrifices I would certainly not have been blessed with the many opportunities that led to this one. Any and all of my successes are possible because they care for (and sometimes spoil) me.

Thirdly, I would like to express my genuine gratitude to my undergraduate physics cohort without whom I would not have had as pleasant nor successful an undergraduate experience. Conversely, I would like to thank my Naval Academy roommates and the friends that I have made in the past six years of my academic career. In addition to turning unfortunate experiences into hilarious memories that I will never forget, they have equipped me with the ability to analyze life's problems through the lenses of multiple perspectives, and tackle life's challenges with unwavering resilience.

Lastly, thank you to the United States Naval Academy (USNA) Admiral Frank Bowman Scholarship program and all the USNA professors whose efforts provided me with the technical foundation to compete for said scholarship. From a teenager with low SAT scores and poor math and science records, this opportunity has been a transformation (starting at the Naval Academy Preparatory School) that has changed my life for the better. I hope that more junior officers will take advantage of it. To all those young Naval Academy midshipmen struggling through math, science, and engineering courses: be patient and open-minded, and stay the course—the best is yet to come.

THIS PAGE INTENTIONALLY LEFT BLANK

I. INTRODUCTION

The United States Navy (USN) is highly interested in the deployment of high-energy lasers (HELs) onboard naval platforms [1], [2]. Their various advantages over conventional weapons make them highly plausible additions to the U.S. Navy's weapon arsenal; these advantages include low-cost per engagement, speed of light payload delivery, graduated output power for hard or soft kills, and potential swarm-defense capabilities [3]. However, due to their high initial overhead costs and because they are a new technology, it is important to fully understand both their strengths and limitations to ensure that investments lead to building an optimal weapon.

Unlike conventional weapons, HEL effectiveness varies strongly with the weather and atmosphere conditions. Parameters like pressure, humidity, temperature, aerosol content, and turbulence can drastically affect the attenuation of the laser light and thus the power delivered to the target [4]. Therefore, it is critical to build HELs that lase at wavelengths that are within the optimal ranges for propagation. In order to be confident that optimal conditions are met, it is important that physics-based simulations be compared to experimental data, where available. Reliance solely on either could lead to an HEL operating at an effective range that is less than expected.

The first part of this thesis will describe the history of HELs and the main types of lasers along with their advantages and disadvantages. The next part will provide an overview of the atmospheric parameters that affect HEL propagation. Then, a simulated example of an HEL near a potential operational theater will be used to illustrate the effects that different climates can have on HEL propagation. Finally, an experimental setup employing a White cell (WC) will be constructed for the purpose of measuring the attenuation in the atmosphere; first results from this setup will also be reported.

THIS PAGE INTENTIONALLY LEFT BLANK

II. DIRECTED ENERGY WEAPONS OVERVIEW

Lasers (light amplification by stimulated emission of radiation) have many modern-day uses. They can be used to cut metals, track targets, read barcodes at supermarkets, among other tasks [5]. A laser is generally composed of a power supply, a gain medium where the light is generated and amplified, and an optical cavity consisting of one partially reflecting mirror and one fully reflecting mirror [6]. There is also a pump stored in the optical cavity that excites electrons in the gain medium, leading to spontaneous and stimulated emission of photons.

The first laser was constructed by Theodore Maiman in 1960. It used a ruby crystal as a gain medium and provided less than 1 watt of output power [6]. The pump used was a quartz flash tube as labelled in Figure 1. By the end of the 1960s, lasers delivering approximately 100 kilowatts (KW) of output power had been produced [4].

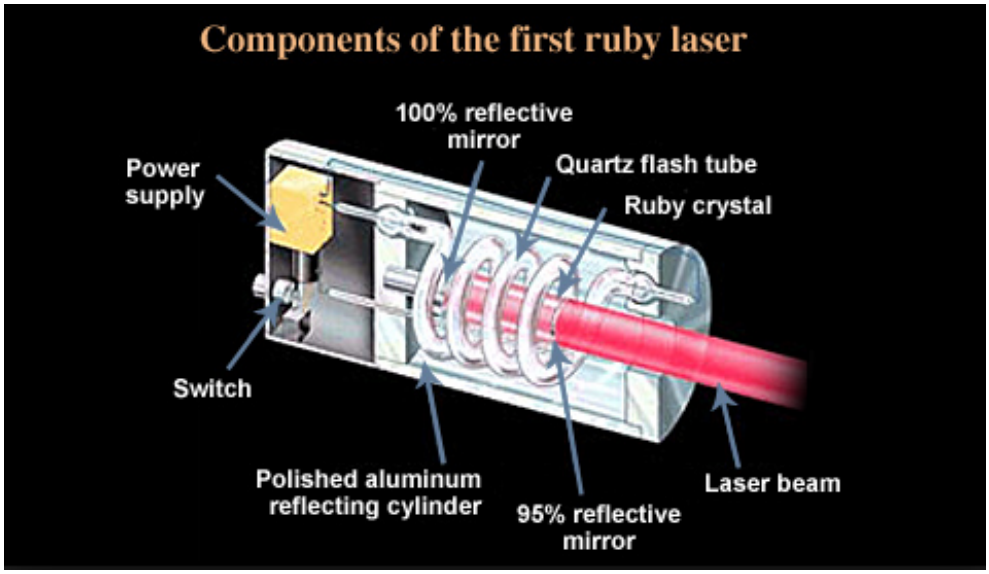

Figure 1. Components of the first ruby laser. From [6].

From the 1970s to the early 2000s, the USN and U.S. Air Force (USAF) experimented with kilowatt and megawatt class deuterium fluoride, carbon dioxide, and oxygen iodine chemical lasers [4]. The USAF ran tests on aerial platforms while the USN tested both static and moving ground-based platforms like the high mobility multi-purpose wheeled vehicle (HMMWV) [4]. During this period, the primary mission for both was to acquire the capability of shooting down missiles; these projects achieved success on more than one occasion in test settings [4].

These early HEL tests used reactive chemical magazines that made them less than ideal for deployment on ships; for this reason, the USN is currently pursuing other laser technologies, including solid-state and free electron lasers. In 2014, the USS *Ponce* (LPD-15) deployed with the Laser Weapon System (LaWS), a 30 kW solid-state fiber laser, and in doing so became the first USN ship to deploy to an operational theater with an HEL [7].

A. ADVANTAGES OF HELS

HELs harness many exclusive advantages over conventional weapons. They are capable of delivering their payload from several kilometers away, depending on weather conditions [8]. Even at this range, the beam spot size on the target is roughly 10 cm in diameter, so collateral damage is limited. Additionally, the amount of power delivered can be adjusted to produce a "soft" kill. A soft kill is when a target is neutralized or disabled but not necessarily destroyed [4]. Lasers also deliver energy at the speed of light, whereas bullets and missiles take time that potentially allows the target to undergo evasive maneuvers.

Furthermore, the HEL technologies the USN is currently pursuing are completely electric, which means that the magazine is limited only by available power. This also means there are no explosives or reactive chemicals involved, improving overall safety. Cost is another advantage, since the amount of energy needed for a typical 10-second laser engagement can be obtained from about a gallon of the ship's fuel [4]. This is quite an advantage when one considers that a rolling airframe (RAM) missile engagement costs

~$1.0 million and a phalanx close-in weapon system (CIWS) missile engagement is ~$3,000 [9], [10].

B. DISADVANTAGES OF HELS

On the other hand, there are some complications that come with HELs. The main limitation is that the overhead cost to build them can be considered quite high—especially when compared to their conventional counterparts. Additionally, energy storage banks (such as batteries or capacitors) will likely be needed to store enough energy for multiple engagements. This requires additional cost, space, and weight. Also, HEL propagation relies heavily on the composition of the atmosphere, which can significantly limit the power reaching the target in less than ideal conditions, such as hazy or turbulent weather [4].

HELs will likely never be the sole means of defense for a USN ship. However, HELs seem to have a substantial superiority over conventional weapons in many cases—a superiority that could solidify their place aboard USN ships as a compliment to conventional weapon systems.

C. HEL TECHNOLOGY

The type of laser employed in a scenario depends, among other things, on the amount of optical power needed to destroy a target. The ability of an HEL to neutralize or destroy a target is largely dependent on the material of the target, the amount of energy delivered by the HEL to the target, over what time that energy is delivered, and over what area on the target that energy is focused. The principal means of lethality is depositing large amounts of thermal energy on a focused point with the intent of penetrating the material by burning or melting it [4].

For example, light aircraft skin consists of approximately 1 mm thick aluminum. To melt a ~100 cm^2 hole in this material within a few seconds requires an energy deposition rate on the order of several tens of kilowatts [9]. Solid-state lasers (SSLs) can achieve this output power; for example, the 30 kW LaWS device is comprised of solid-state fiber lasers.

On the other hand, a harder target such as a cruise missile may require the removal of approximately 1 liter of bulk aluminum before it is disabled. In that case, a megawatt class laser would be required to affect this amount of damage within a few seconds [9]. Free electron lasers (FELs) are thought to be scalable more easily than SSLs to this level of output power.

1. Solid-State Lasers

SSLs use dopants like neodymium and ytterbium held by substrates like glass or crystal as a lasing medium [4]. Inside the dopant are the electrons that will undergo lasing transitions as they release the photons that make up the beam. Due to possible damaging of the substrate, SSLs are likely limited in output power to several tens of kilowatts, and even then only by combining the beams from multiple lasers [9]. Additionally, the lasing wavelength for SSLs is fixed by the gain medium and may not fall within an atmospheric window where attenuation is minimized [1]. Nevertheless, the SSL is a relatively compact, mature, and power-efficient technology that does not produce harmful chemicals or radiation.

2. Free-Electron Lasers

As opposed to their solid-state counterparts, FELs use free electrons as opposed to substrates with bound electrons. They operate by first accelerating these free electrons in a linear accelerator (LINAC) to relativistic energies. The electrons are then fed through a periodic magnetic field that causes the electrons to “wiggle” back and forth, thereby producing photons [4]. Further interactions between the electrons and the light field cause the electrons to bunch on the scale of the optical wavelength; the combination of wiggling and bunching results in stimulated emission of coherent light [4]. A diagram of an FEL that uses an energy recovery LINAC (ERL) (to increase wall-plug efficiency) is depicted in Figure 2.

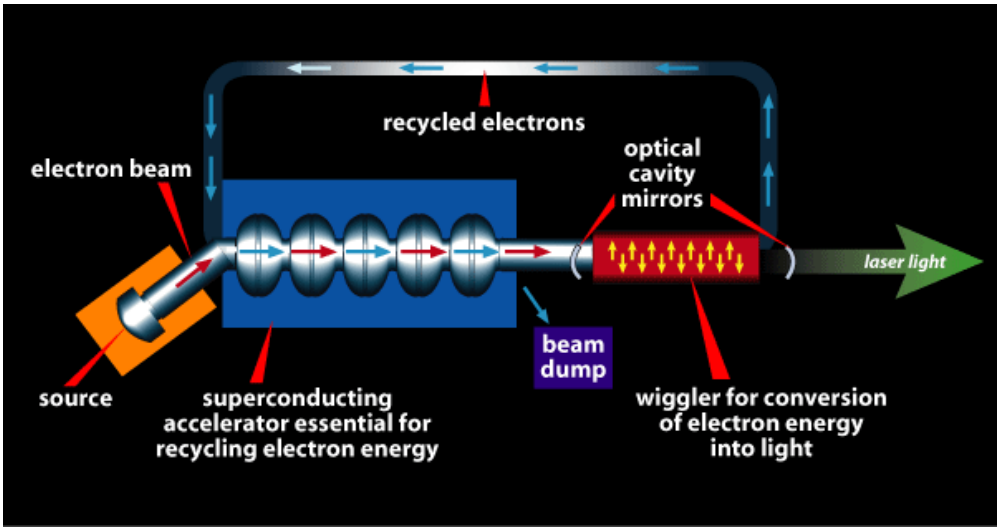

Figure 2. The basic components of an FEL with an ERL. The electrons are extracted from a source, accelerated to relativistic speeds in the LINAC, "wiggled" in magnetic fields to prompt the release of photons, and recycled back into the linear accelerator to be decelerated, where their kinetic energy is recycled back into the system, before being dumped. From [11].

FELs tend to be rather large (about 20 meters long), heavy, and expensive [1]. They also require shielding from the radiation produced from the relativistic electrons. However, they feature arbitrary wavelength selection, which means that they can be designed for ideal atmospheric transmission and, in principle, tune their wavelengths depending on the atmospheric conditions. FELs also have no substrate to damage, so they are believed to be scalable to higher output powers than SSLs (~ megawatts) while retaining excellent beam quality [4]. FELs are not as technically mature as SSLs, but they may make an attractive choice for future laser weapons.

D. HEL MISSIONS AND PLATFORMS

The naval missions that HELs would be used for depend heavily on their output power level. HELs on the order of tens of kilowatts could successfully neutralize slow-moving targets like boats and small watercraft in addition to light planes and aerial drones. They could even be used for 'soft' kills against missiles by blinding their seeker. On the other hand, HELs with megawatt-level output power could be used to disable supersonic missiles.

Both classes of lasers could be equipped to various ship platforms including littoral combat ships (LCS), Arleigh Burke (DDG-51) and Zumwalt (DDG-1000) class destroyers, Nimitz (CVN-68) and Ford (CVN-78) class aircraft carriers, and future all-electric ships [11]. The USN is even considering putting HELs on Virginia class submarines, to defend against potential surface or airborne threats. Additionally, the USN and United States Marine Corps have considered deploying HELs on aircraft [11], [12].

III. ATMOSPHERIC PROPAGATION OVERVIEW

As light propagates through a medium, there are two primary ways that it can interact with matter. One way is for the photons to be absorbed by the particles in the medium as they excite electrons to higher energy levels. This encounter is inelastic since energy is removed from the light field and the temperature of the atmosphere increases. Another is that the photons can scatter off of the particles in the medium, similar to the balls on a billiards table hitting one another. In this case, temperature is not appreciably increased since the interaction is approximately elastic. As the photons interact with matter, the overall intensity of light is decreased because these interactions remove energy from the laser beam. This attenuation is governed by Beer's Law, named after German physicist August Beer [13].

A. ATMOSPHERIC EXTINCTION

Beer's Law combines the factors that account for the attenuation of electromagnetic waves into a single coefficient and relates *P*, the power reaching an area at a distance *z* from the source, to the initial power P_o through a decaying exponential [13]:

$$P(z) = P_o e^{-\epsilon z} . \tag{1}$$

The coefficient ϵ is known as the 'extinction coefficient' which is mathematically defined as the number of particles per unit volume, *N*, multiplied by the effective cross sectional area of the particles the light is passing through, σ:

$$\epsilon = N\sigma . \tag{2}$$

There are two main types of particles in the atmosphere that contribute to the extinction coefficient: molecules and aerosols. Aerosols are larger particles, and can have more complex structures like dust, sand, fog, etc. To facilitate calculating the contributions of aerosols and molecules, the extinction coefficient is generally broken down into different components. As such, it takes the following form:

$$\epsilon = \alpha_m + \alpha_a + \beta_m + \beta_a . \tag{3}$$

Equation (3) differentiates between absorption and scattering by using the variables α and β, respectively. Additionally, the subscript m stands for molecules while the subscript a represents aerosols. Each of these components is well-defined, can be measured or estimated via calculations, and is a function of the light wavelength.

1. Molecular Absorption

As can be seen in Table 1, air at standard conditions is mostly composed of diatomic nitrogen and oxygen molecules. However, the symmetric vibrational modes of these two molecules do not couple strongly to infrared light because homonuclear diatomic particles do not exhibit changes in their dipole moments. For this reason, these two species have negligible absorption in this region of the spectrum [14]. Instead, water vapor (H_2O) and carbon dioxide (CO_2), which together make up only a small fraction of ambient air, are mainly responsible for the complicated absorption features in the infrared portion of the electromagnetic spectrum [14]. In order to ensure minimal attenuation, it is imperative to find a wavelength that is not particularly sensitive to CO_2 or H_2O absorption.

The Composition of the Atmosphere[a]

Permanent constituents		Variable constituents	
Constituent	% by volume	Constituent	% by volume
Nitrogen (N_2)	78.084	Water vapor (H_2O)	0–0.04
Oxygen (O_2)	20.948	Ozone (O_3)	0–12 × 10^{-4}
Argon (Ar)	0.934	Sulfur dioxide (SO_2)[b]	0.001 × 10^{-4}
Carbon dioxide (CO_2)	0.036	Nitrogen dioxide (NO_2)[b]	0.001 × 10^{-4}
Neon (Ne)	18.18 × 10^{-4}	Ammonia (NH_3)[b]	0.004 × 10^{-4}
Helium (He)	5.24 × 10^{-4}	Nitric oxide (NO)[b]	0.0005 × 10^{-4}
Krypton (Kr)	1.14 × 10^{-4}	Hydrogen sulfide (H_2S)[b]	0.00005 × 10^{-4}
Xenon (Xe)	0.089 × 10^{-4}	Nitric acid vapor (HNO_3)	Trace
Hydrogen (H_2)	0.5 × 10^{-4}	Chlorofluorocarbons	Trace
Methane (CH_4)	1.7 × 10^{-4}	($CFCl_3$, CF_2Cl_2	
Nitrous oxide (N_2O)[b]	0.3 × 10^{-4}	CH_3CCl_3, CCl_4, etc.)	
Carbon monoxide (CO)[b]	0.08 × 10^{-4}		

[a] After the U.S. Standard Atmosphere (1976) with modifications.
[b] Concentration near the earth's surface.

Table 1. Air composition at standard conditions. From [14].

The molecular absorption spectrum for wavelengths between 0.5μm and 5μm is shown in Figure 3. The peaks in the graph are indicative of wavelengths where the molecular absorption coefficient is particularly large and not suitable for atmospheric propagation. Note that the y-axis uses a logarithmic scale, making these peaks much more significant.

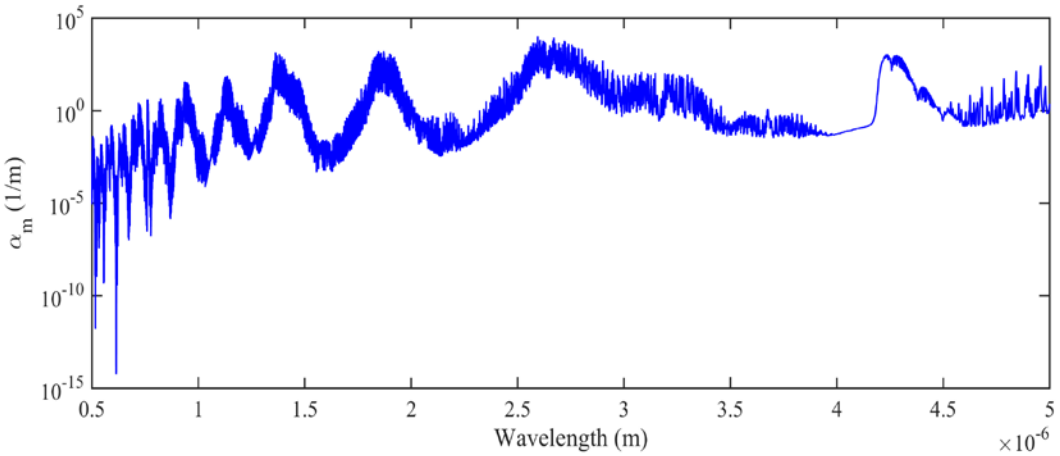

Figure 3. Typical plot of the molecular absorption spectrum from 0.5μm to 5μm. Made using the Laser Environmental Effects Definition and Reference (LEEDR) atmospheric codes. The molecular absorption coefficient has a very strong dependence on wavelength. After [15].

B. BROADENING MECHANISMS

A light/molecule interaction can be approximated as a classically damped harmonic oscillator, modeled by the following equation [14]:

$$F = qE = m_e\ddot{x} + 4\pi m_e \Gamma_n \dot{x} + kx \, . \tag{4}$$

In Equation (4), q is the charge of the electron undergoing the interaction, E represents the effective electric field of the light source exciting said electron, m_e is the mass of the electron, k represents the effective spring constant and is related to how tightly the electron is bound to the molecule, and Γ_n represents the effective damping from photon emission as the electron returns to the non-excited state. This equation can be used to determine the imaginary component of the refractive index of the system of

molecules that is responsible for the molecular absorption coefficient [14]. The normalized functional line shape for this coefficient, $\alpha_m \propto f(\nu - \nu_o)$, is then defined by:

$$f(\nu - \nu_o) = \frac{1}{\pi} \frac{\Gamma_n}{(\nu - \nu_o)^2 + {\Gamma_n}^2} \quad , \tag{5}$$

where ν is the light frequency and ν_o is the central frequency of the line which is related to the energy difference between the levels the electron is transitioning between. This shape is a Lorentzian whose thickness depends upon the damping factor Γ_n. The larger Γ_n is, the broader the spectral line width for that particular transition. Figure 4 shows the effects of damping and frequency on spectral line width.

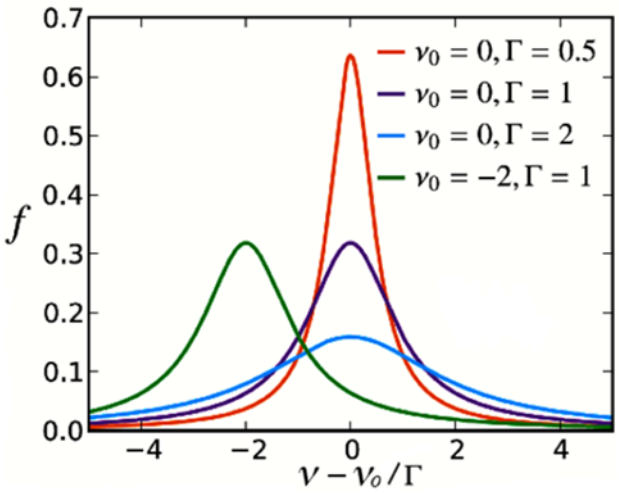

Figure 4. Resonant frequency and the damping dependence of the spectral line width. From [16].

It is of interest to note that the Γ_n value is related to the transition rate between quantum energy states. This is governed by Fermi's Golden Rule and is related to the initial and final energy states and the perturbing Hamiltonian [14]. The overall absorption coefficient as a function of frequency for a molecular species is then the sum over all transitions in the molecule where each single transition has the functional form of $f(\nu - \nu_o)$.

For an isolated molecule, Γ_n values are on the order of 0.3 Hz—small compared to the light frequency, which is on the order of 10^{15} Hz. Therefore, absorption lines

should be very narrow based upon this simple analysis; however, measurements show that they are actually much broader. There are two primary mechanisms that account for this extra broadening of spectral lines.

1. Pressure/Collision Broadening

Pressure broadening occurs when collisions between molecules produce an enhanced damping effect. Colliding molecules transfer energy which leads to a shorter lifetime in their excited state, thus enhancing the damping. This collision damping is on the order of Γ_P~10^8 Hz, which dominates the absorption line width as it is much greater than the Γ_n value of ~0.3 Hz. Increasing pressure causes more frequent collisions and thus broader Lorentzian absorption lines. The physical effects of pressure broadening can be quantified by the following relationship:

$$f_P(\nu - \nu_o) = \frac{\Gamma_P/\pi}{(\nu-\nu_o)^2+{\Gamma_P}^2} \ , \tag{6}$$

where Γ_P is the effective damping constant that accounts for the collisions. This constant is dependent on the average time between inelastic molecular collisions t_c in the following way:

$$\Gamma_P = \frac{1}{2\pi t_c} \ . \tag{7}$$

Figure 5 shows an example of the effects of pressure on the broadening of the spectral lines.

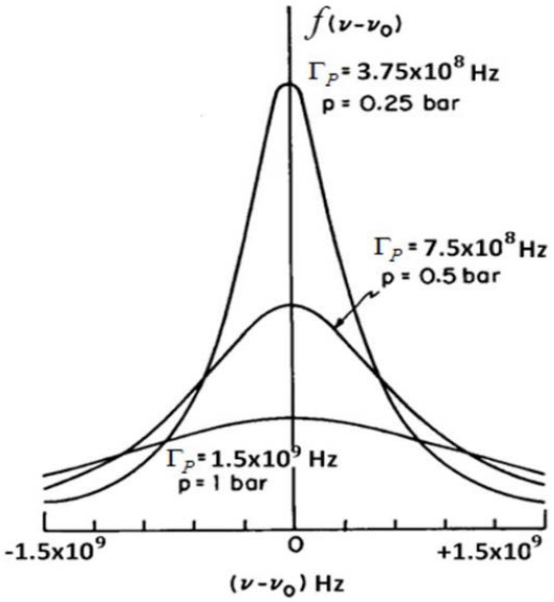

Figure 5. Increasing pressure makes the spectral lines broader because of the decrease in the average time between collisions. From [17].

2. Doppler Broadening

As photons propagate through a set path, they encounter molecules traveling with random velocities. Approximately half of them have a component of their velocity moving towards the source while the other half will have a component of their velocity moving away from the source. Similar to the way the sound frequency of an ambulance changes depending on whether it is traveling away from or toward the observer, the absorption spectrum gets blue-shifted and red-shifted because of the molecules moving towards and away the source, respectively. This effect adds a Gaussian shape to an absorption feature described by the following relationship [18]:

$$f_D(\nu - \nu_o) = \frac{1}{\Gamma_D\sqrt{\pi}} exp\left[-\frac{(\nu-\nu_o)^2}{{\Gamma_D}^2}\right], \tag{8}$$

$$\Gamma_D = \nu_o\sqrt{\frac{2k_BT}{mc^2}}, \tag{9}$$

where Γ_D is the Doppler line half-width, k_B is the Boltzmann constant, c is the speed of light in vacuum, m is the mass of the molecule, and T is the absolute temperature. As can

be noted in Equation (9), an increase in temperature produces a broader spectral line because of this Doppler shift.

3. Voigt Profiles

In order to combine the effects of pressure and Doppler broadening, atmospheric simulation codes use Voigt profiles, which are defined by the following relationship [17]:

$$f_V(\nu - \nu_o) = \frac{\Gamma}{\Gamma_D \pi^{3/2}} \int_{-\infty}^{\infty} \frac{e^{-y^2}}{(x-y)^2 + \Gamma^2} dy \ , \tag{10}$$

where $\Gamma \equiv \Gamma_P / \Gamma_D$ and $x \equiv (\nu - \nu_o)/\Gamma_D$. The Voigt profile is shown in Figure 6.

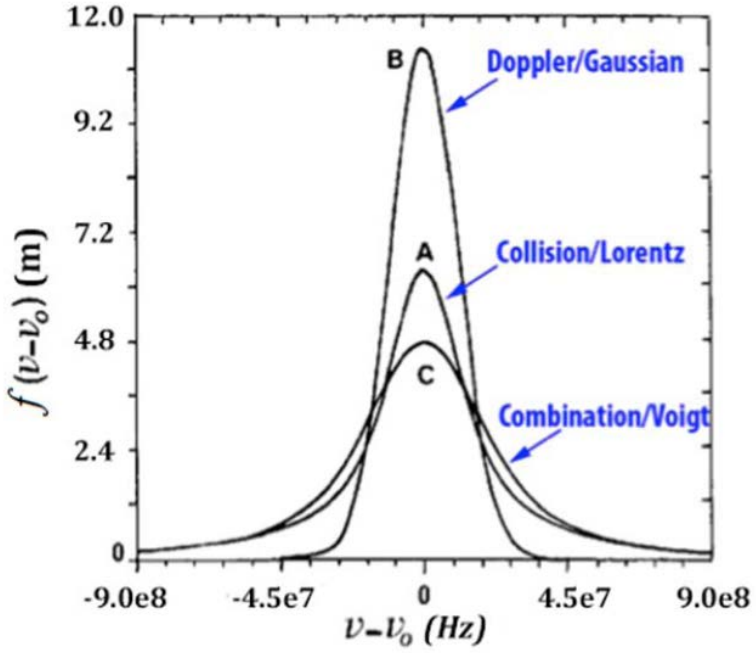

Figure 6. Voigt profiles resemble Gaussian shapes near resonance ($\nu \cong \nu o$) and Lorentzian shapes far from resonance. From [17].

Voigt profiles resemble Gaussian shapes near resonance ($\nu \cong \nu o$) and Lorentzian shapes far from resonance. Similarly, they more closely resemble Lorentzian line shapes when collision broadening dominates (as it does near the surface), and more closely resemble Gaussian line shapes when Doppler broadening dominates (at higher altitudes).

However, each Voigt profile describes the absorption features for a single molecular transition. The overall absorption spectrum of the atmosphere is a summation

of Voigt profiles for each absorption line as shown in Figure 7. It is important to note that the wavelength range depicted spans only 0.01nm, yet the spectrum is very intricate and contains dozens of absorption features.

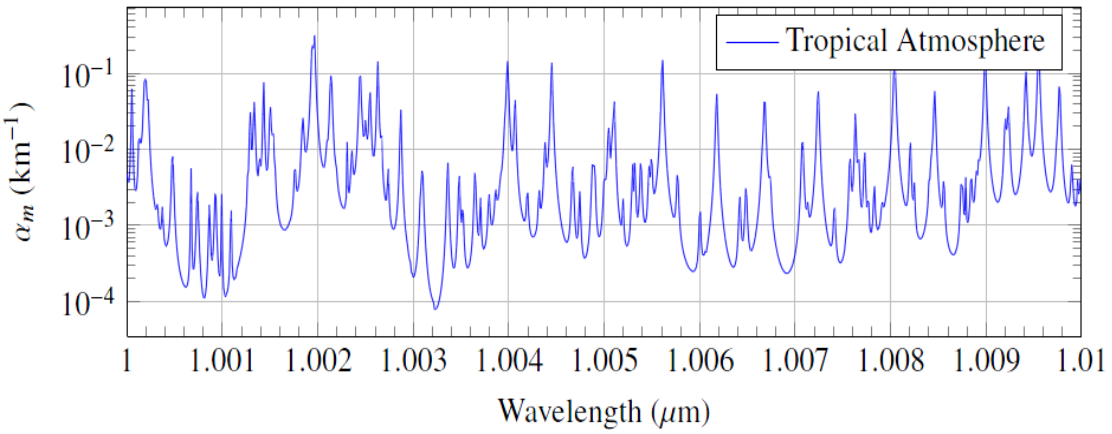

Figure 7. Typical plot of the molecular absorption coefficient from 1μm to 1.01μm. Made with high-resolution transmission (HITRAN) molecular absorption database atmospheric codes. Note the dozens of Voigt profiles necessary to map out a 0.01μm range. From [19].

4. Continuum Absorption

Voigt profiles represent spectral features relatively well near resonances. However, in windows of weak absorption, an additional component must be added. Continuum absorption is the difference between the Voigt profile simulations and actual measurements made at the simulated conditions and can contribute significantly to the absorption in regions of the spectrum where the absorption is otherwise weak.

The causes for continuum absorption are still debated, but it has relatively weak dependence on wavelength. It is, however, sensitive to temperature and pressure. One theory is that continuum absorption is due to errors in the calculated spectrum formed by summing over Voigt profiles. Another hypothesis attributes continuum absorption to water dimers (two or more water molecules bound by a hydrogen bond) [20]; the disassociation energy of these dimers is unaccounted for in the Voigt profiles. Whatever the cause, continuum absorption must be factored in when determining the absorption coefficient, α_m, especially for regions of the spectrum between strong absorption features.

C. MIE SCATTERING

Mie scattering theory describes light interacting with small particles like dust, and sand, and accounts for the other three components of the extinction coefficient: aerosol absorption, aerosol scattering, and molecular scattering. Mie scattering theory makes three assumptions. The first is that the scattering particles are spherical with radius *a*. The second is that these scattering particles are homogeneous with a complex refractive index [21]. Finally, Mie scattering theory assumes that light is a plane wave. As it turns out, this assumption is good when particles are much smaller than the beam cross section, which is valid in the case of laser propagation [21]. From these assumptions, we can put together an amplitude scattering matrix to help solve for the three components of the extinction coefficient previously listed [22].

1. Rayleigh Scattering

The Raleigh scattering limit to Mie scattering occurs when the radius of the scattering particle is much smaller than the wavelength of the incident light. This limit is valid for molecular scattering. Figure 8 shows the molecular scattering spectrum for the wavelength range of 0.5μm to 5μm.

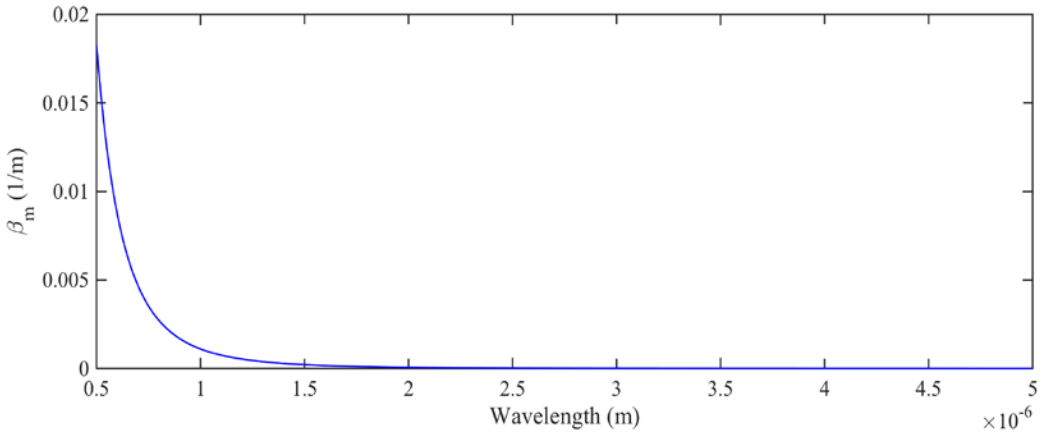

Figure 8. Typical plot of the molecular scattering spectrum from 0.5μm to 5μm. Made using LEEDR. Note the exponential increase in scattering at shorter wavelengths. After [15].

Figure 8 shows that shorter wavelengths of electromagnetic radiation are correlated with higher levels of molecular scattering—a known feature of Rayleigh scattering. In practice, this explains why the sky is blue: blue light undergoes molecular scattering more readily than red light [14].

2. Aerosol Effects

Aerosol sizes are comparable to the wavelength of the scattered light; therefore, full Mie theory must be used as opposed to sticking to the Raleigh approximation [23]. In Figures 9 and 10, typical aerosol absorption and scattering spectra are shown for the wavelength range 0.5μm to 5μm. Note the logarithmic scale used for the aerosol absorption values.

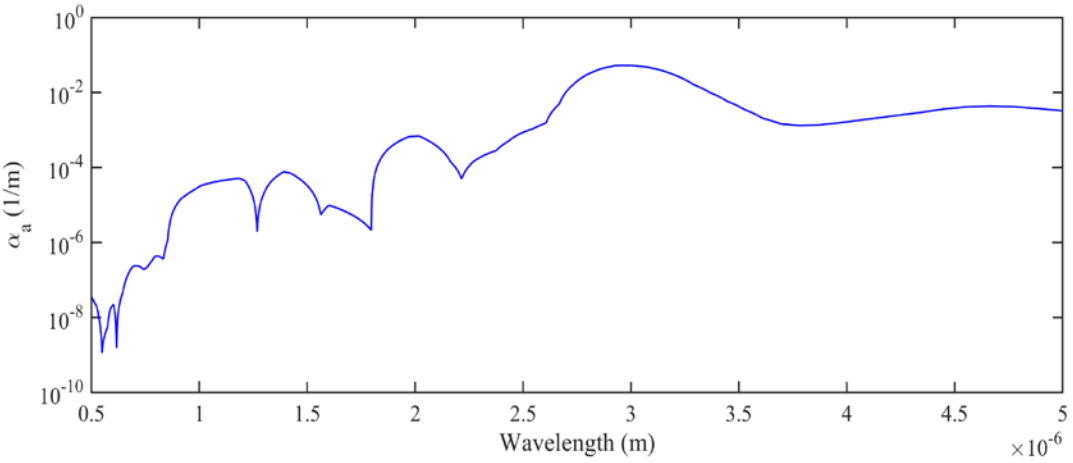

Figure 9. Typical plot of the aerosol absorption spectrum from 0.5μm to 5μm. Made with LEEDR atmospheric codes. Notice the relatively weak dependence on wavelength. After [15].

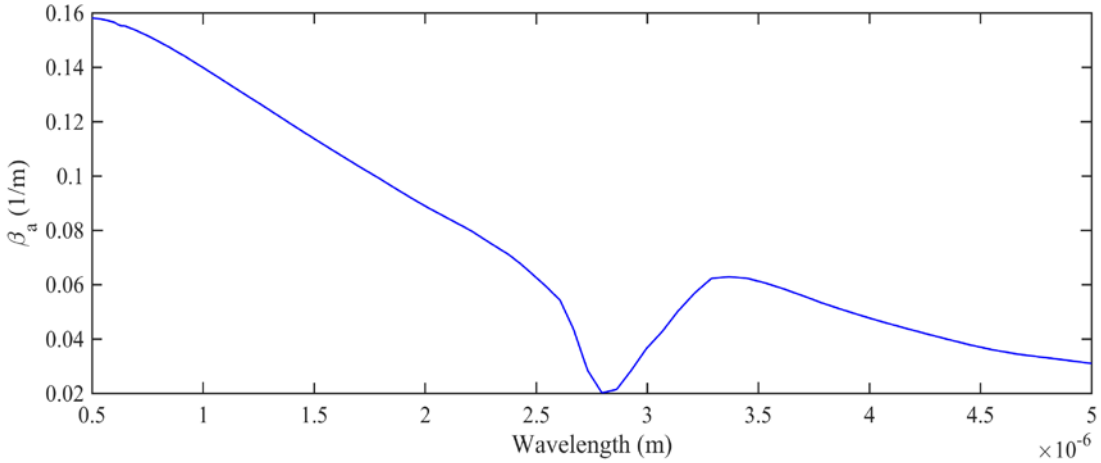

Figure 10. Typical plot of the aerosol scattering spectrum from 0.5μm to 5μm. Made with LEEDR atmospheric codes. Notice the relatively weak dependence on wavelength. After [15].

As shown, aerosols have relatively weak wavelength dependence for both absorption and scattering in this spectral range [24]. This explains why clouds and fog appear white—they are composed of aerosols that scatter all wavelengths similarly [14].

THIS PAGE INTENTIONALLY LEFT BLANK

IV. CLIMATOLOGICAL EXAMPLE OF HEL PROPAGATION

Before investing a large amount of money and resources into producing a laser weapon system, it is important to fully understand how various conditions may affect its performance. This chapter features simulations that illustrate how weather can drastically alter the performance of laser weapons. Additionally, they show the importance of choosing the optimal wavelength for HEL design through plots made with *ANCHOR* (Atmospheric NPS Code for High Energy Laser Optical pRopagation) [25]. These ANCHOR plots take into account data from an atmospheric propagation code called LEEDR (Laser Environmental Effects Definition and Reference) [25].

A. OVERVIEW OF ANCHOR CODE

ANCHOR is a concise code designed to rapidly explore millions of different parameters related to laser design and weather, among others. Specifically, ANCHOR takes into account wavelength, laser power, beam quality, as well as atmospheric effects like extinction, turbulence, and thermal blooming. It is Matlab-based and uses an accelerated scaling code that incorporates the equations that govern laser propagation. To validate ANCHOR, irradiance simulations were compared to results from Wavetrain, a full diffraction code developed by MZA Associates Corporation [26]. Wavetrain simulates laser beam propagation by solving the paraxial wave equation numerically, in contrast to ANCHOR, which used the aforementioned scaling laws [26]. Thus, Wavetrain has a time resolution that is not present in ANCHOR; nevertheless, in the time-averaged limit where ANCHOR is valid, both codes produce comparable results.

The process of gathering simulated results goes as follows: LEEDR, which is a code developed by the Air Force Institute of Technology (AFIT), is used to produce atmospheric extinction values under varying climates [15]. The values are then used by ANCHOR, which incorporates additional laser and target geometry parameters. By using ANCHOR, plots that detail effective range, for example, can be constructed.

B. SIMULATION PARAMETERS

For this example, the output laser power is 100 kW and the beam director diameter is 0.3 m. Platform jitter has an assumed root-mean-square value of 5.0 μrad. The lasing wavelengths are 1.0642 μm and 1.5314 μm, chosen because they are within the lasing ranges of ytterbium- and erbium-based gain media, respectively, which are used in commercially available fiber lasers. The beam is taken to have a uniform flat-top transverse profile at the laser output rather than a Gaussian profile. The climate data was taken from LEEDR's database for the Dubai International Airport, which was compiled from meteorological sources. The information supplied by LEEDR is specific to the time of day and is incremented in steps of 3 hours. For the purpose of this simulation, the time of day chosen was the 12:00 pm to 3:00 pm (local time) window. These parameters are referenced in Table 2.

Laser output power	100kW
Beam director diameter	0.3m
Platform jitter	5.0 μrad
Wavelengths	1.0642 μm, 1.5314 μm
Beam profile	Uniform
Location	Dubai Intl. Airport
Time of day (local time)	12:00pm-3:00pm
Humidity	Varies
Surface visibility	Varies

Table 2. Laser and atmospheric parameters for the climatological example.

C. DAMAGE CRITERIA

There are a few assumptions related to the damage criteria for this example. First, the target is taken to be a 1.0 mm thick sheet of aluminum (approximately the thickness of aircraft skin). The estimated dwell time is 10 seconds, the approximate laser spot radius is 5.0 cm, and it is assumed that only 10 percent of the laser light incident onto the target is absorbed by the target. Loss mechanisms, including conductive losses from the transferring of heat away from the target into the surrounding aluminum and radiative

losses from thermal energy being converted to light as the target gets hotter (and emits like a blackbody), are accounted for. All the aforementioned parameters considered, the minimum irradiance needed would be approximately 5 MW/m^2 or 0.5 kW/cm^2 [27]. Note that in most cases the effective range is a strong function of the target altitude. This is often due to stronger turbulence near the surface.

D. RESULTS

In the following figures, the effective range of the 100 kW laser described in section II of this chapter is highlighted in varying climates. The color gradient is representative of the irradiance delivered on the target, with red representing higher irradiances and blue indicating lower irradiance values. It is important to note that this irradiance color scale is logarithmic. The black line delineates the estimated effective range based on the irradiance threshold of 5 MW/m^2 outlined in section III of this chapter. The horizontal and vertical axes represent horizontal range and altitude of the target, respectively.

1. Humidity Examples

The first example varies the relative humidity while keeping the surface visibility at a constant 30 km. Humidity primarily affects the molecular absorption component of the extinction coefficient. Figures 11 through 13 show the effective ranges of a 1.0642 μm laser and varying relative humidities at the surface and a constant 30 km surface visibility.

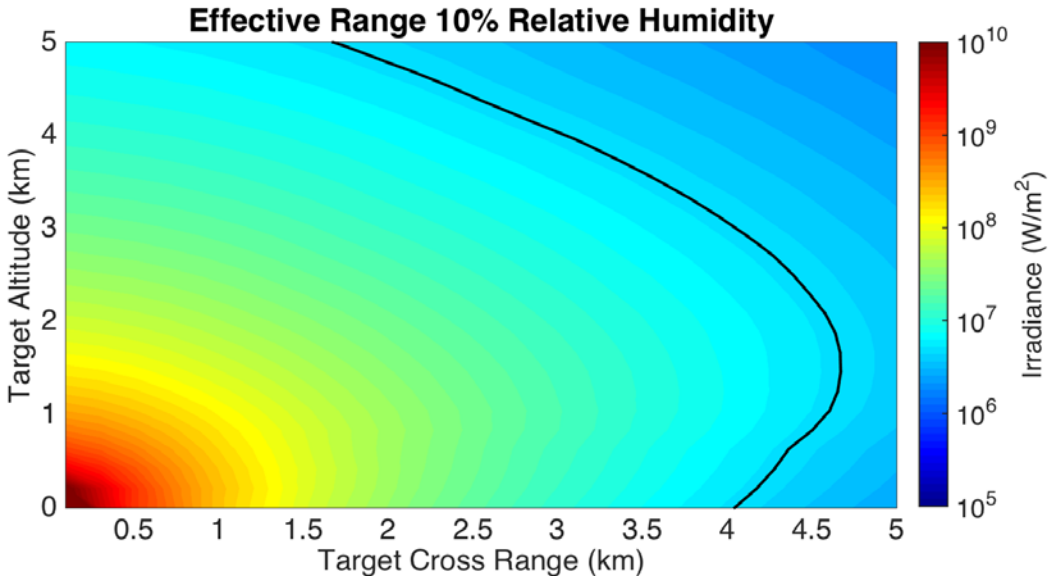

Figure 11. The effective range of a 1.0642 μm laser and a 10 percent relative humidity at the surface. The surface visibility is 30 km.

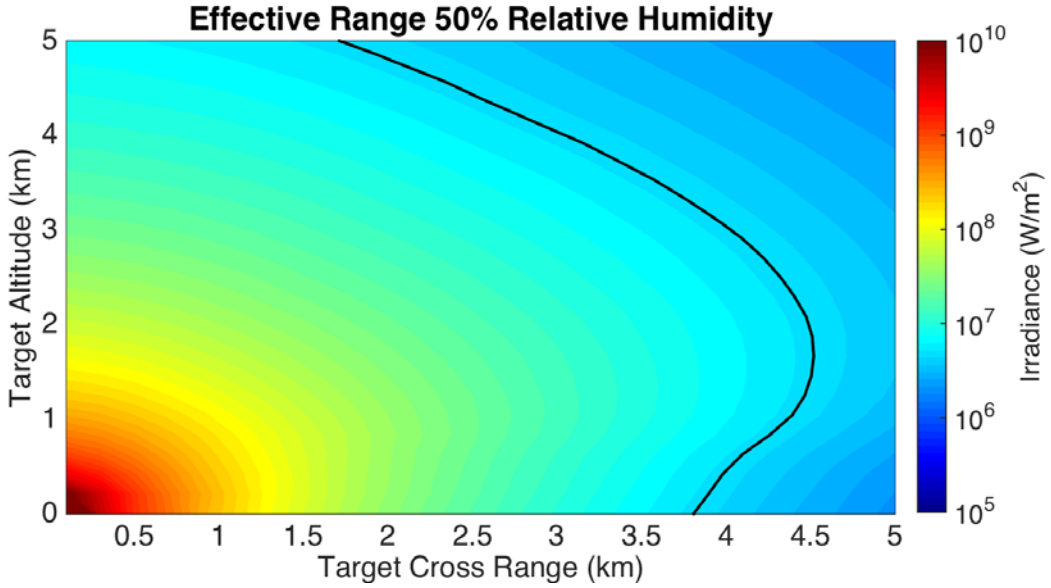

Figure 12. The effective range of a 1.0642 μm laser and a 50 percent relative humidity at the surface. The surface visibility is 30 km.

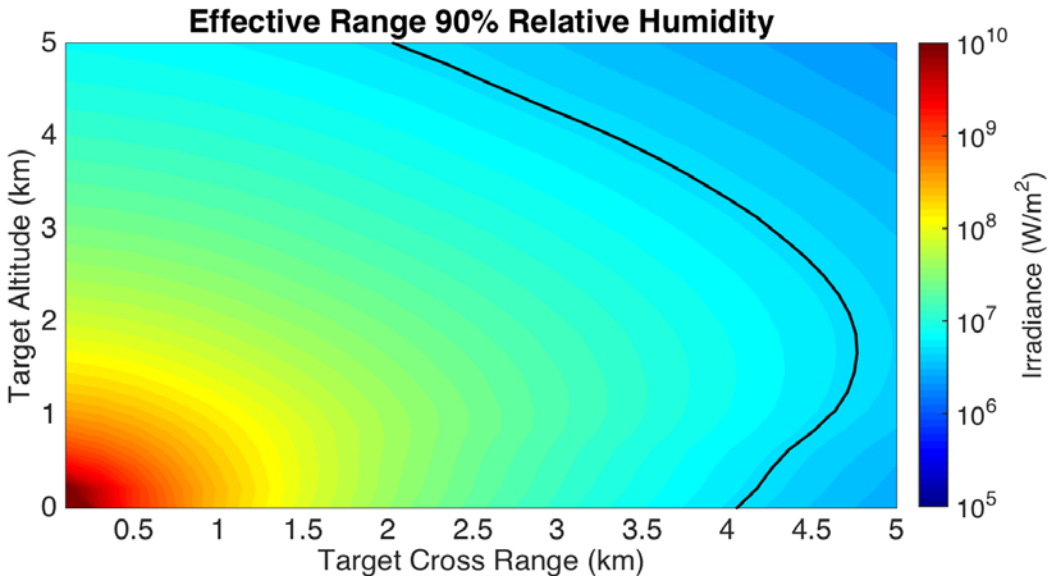

Figure 13. The effective range of a 1.0642 μm laser and a 90 percent relative humidity at the surface. The surface visibility is 30 km.

One will notice that there is very little change in the effective range even with a difference of 80 percent in relative humidity at the surface. In the following graphs, this will not be the case.

Figures 14 through 17 show the effective ranges of a laser with a 1.5314 μm wavelength, 30 km of visibility at the surface, and varying relative humidities at the surface.

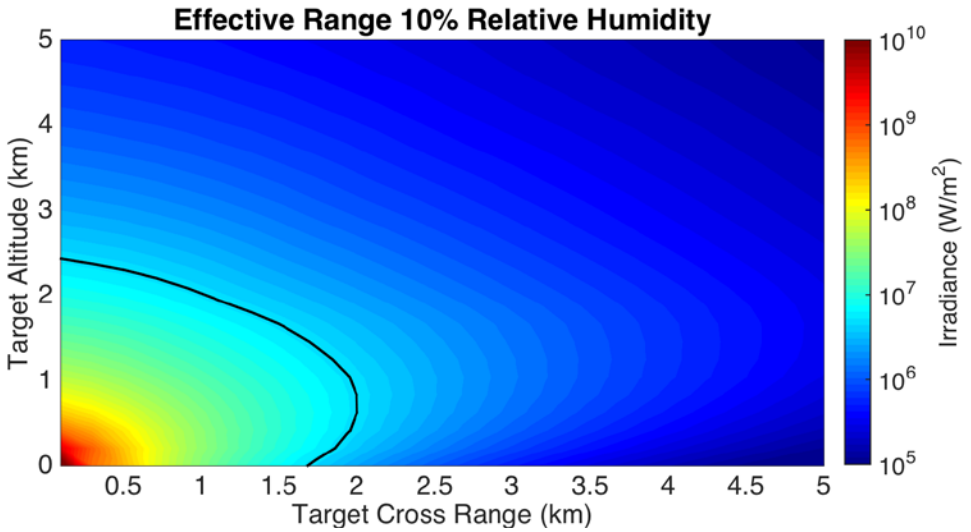

Figure 14. The effective range of a 1.5314 μm laser and a 10 percent relative humidity at the surface. The surface visibility is 30 km.

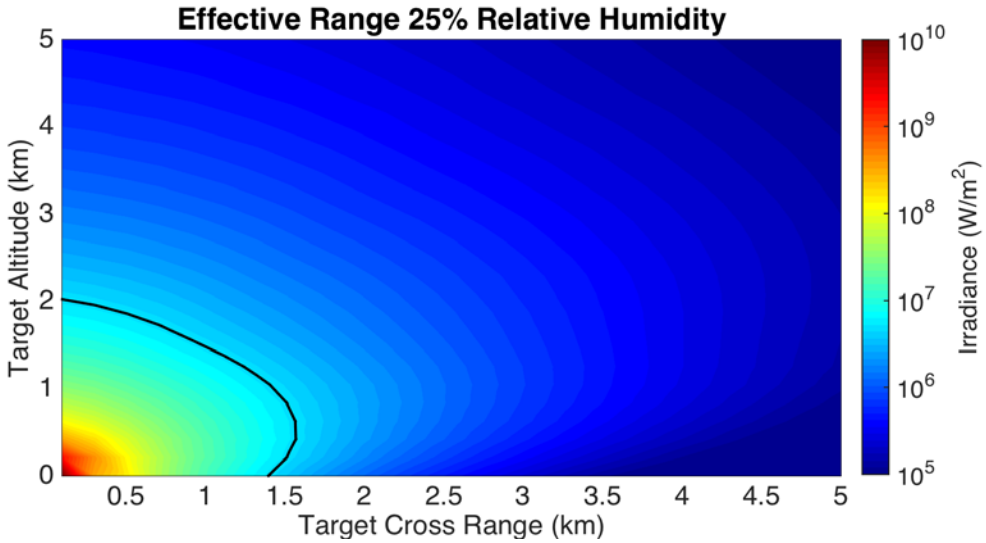

Figure 15. The effective range of a 1.5314 μm laser and a 25 percent relative humidity at the surface. The surface visibility is 30 km.

For this particular wavelength, we can already begin to see the effect that a 15 percent increase in surface humidity has on the laser performance.

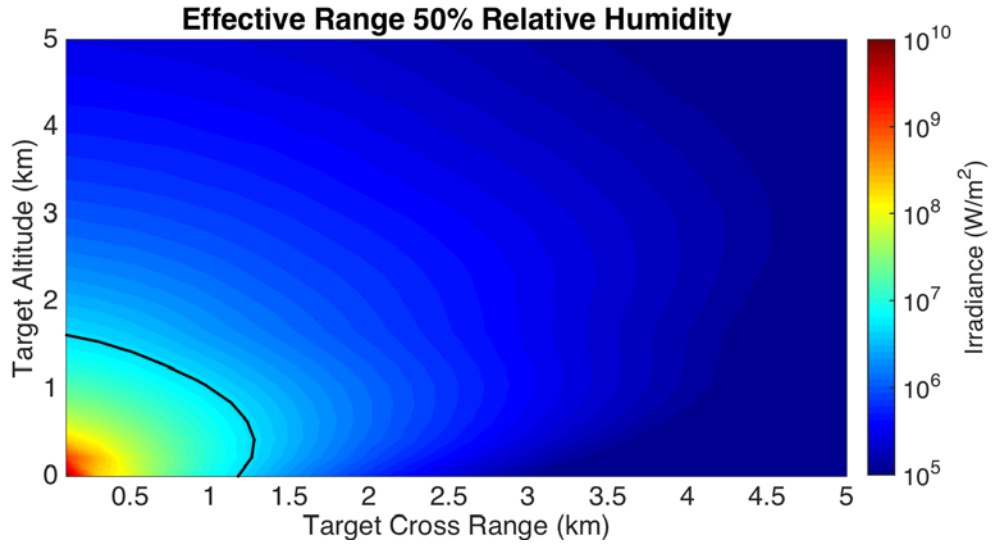

Figure 16. The effective range of a 1.5314 μm laser and a 50 percent relative humidity at the surface. The surface visibility is 30 km.

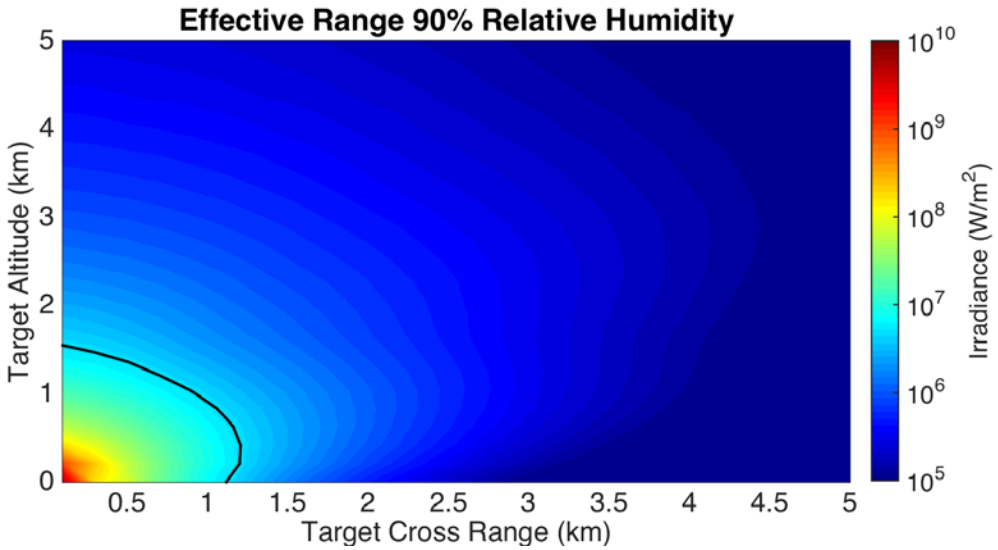

Figure 17. The effective range of a 1.5314 μm laser and a 90 percent relative humidity at the surface. The visibility is held constant at 30 km.

As these graphs show, certain wavelengths can be more sensitive to humidity. In the case of 1.0642 μm there was little effect on molecular absorption. For 1.5314μm however, the effective range with 90 percent relative humidity was almost half of the range at 10 percent relative humidity. It is important to note that the scales and ranges for the vertical and horizontal axes in all the plots remained the same.

2. Surface Visibility Examples

This next example illustrates the effects of holding relative humidity at the surface at a constant 50% and varying the surface visibility. This value for the surface relative humidity was chosen because it is close to the average predicted by LEEDR in the 12:00 pm and 3:00 pm timeslot for a summer day. The visibility is correlated with the aerosol content and thus the attenuation due to aerosol scattering. Figures 18 through 21 show the effective ranges of a 1.0642 μm laser with a constant 50 percent relative humidity at the surface and varying surface visibility.

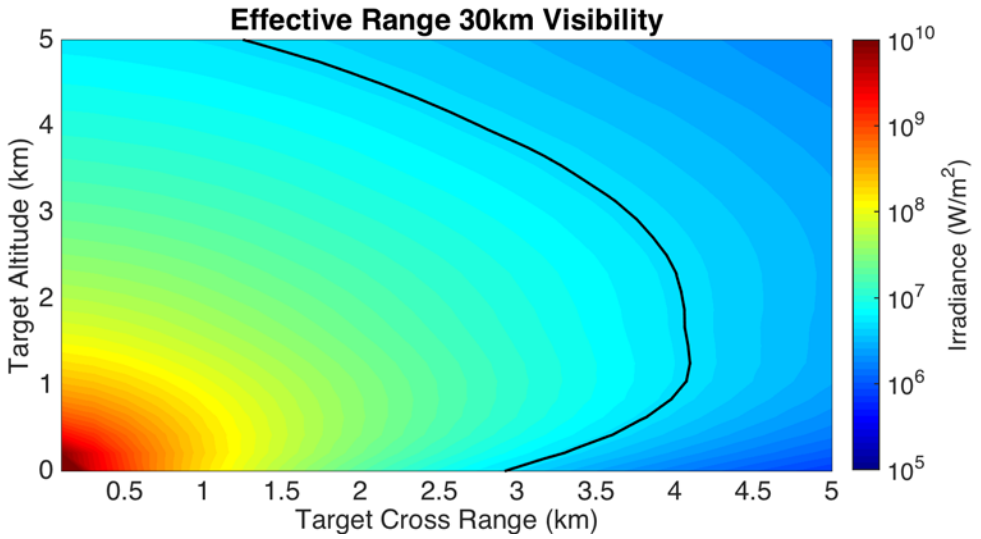

Figure 18. The effective range of a 1.0642 μm laser and 30 km of surface visibility. The relative humidity at the surface is 50 percent.

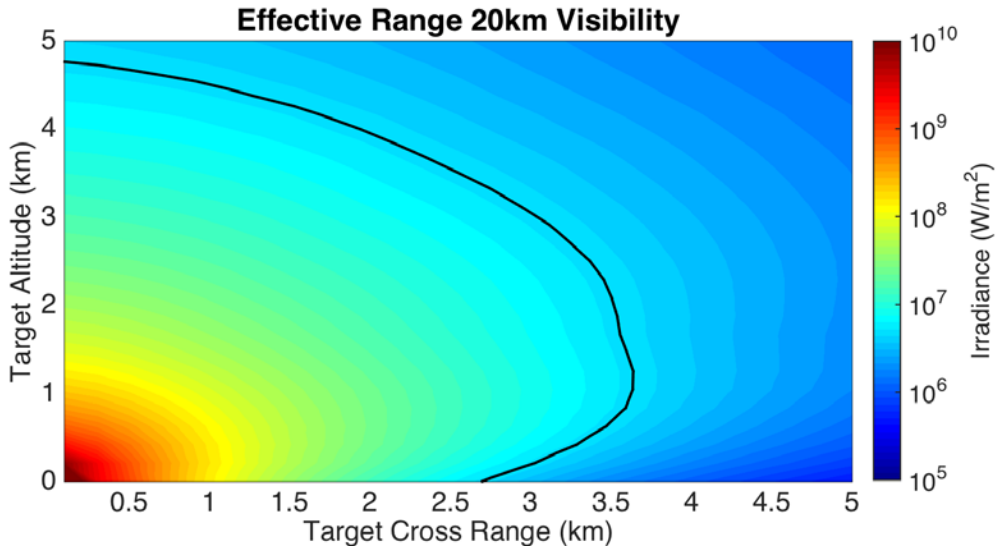

Figure 19. The effective range of a 1.0642 μm laser and 20 km of surface visibility. The relative humidity at the surface is 50 percent.

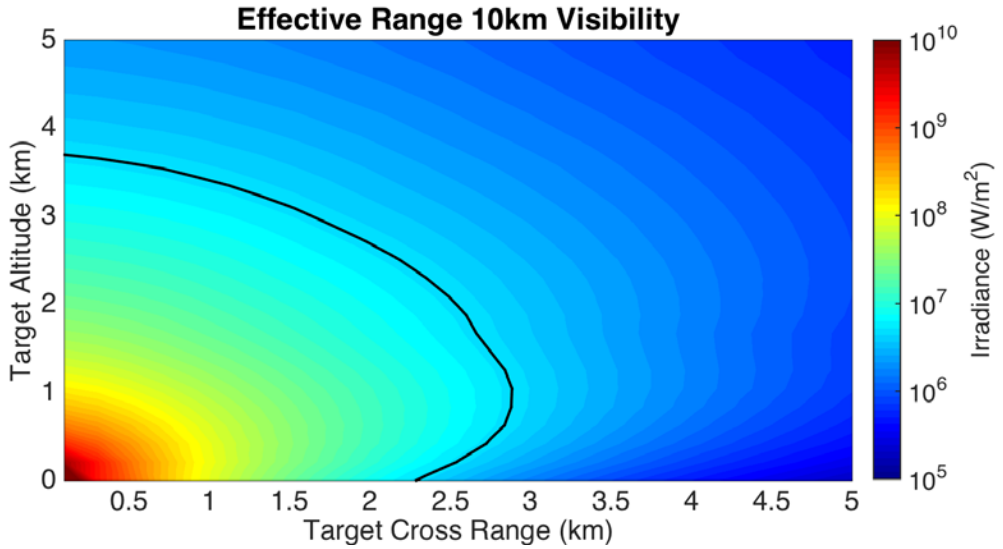

Figure 20. The effective range of a 1.0642 μm laser and 10 km of surface visibility. The relative humidity at the surface is 50 percent.

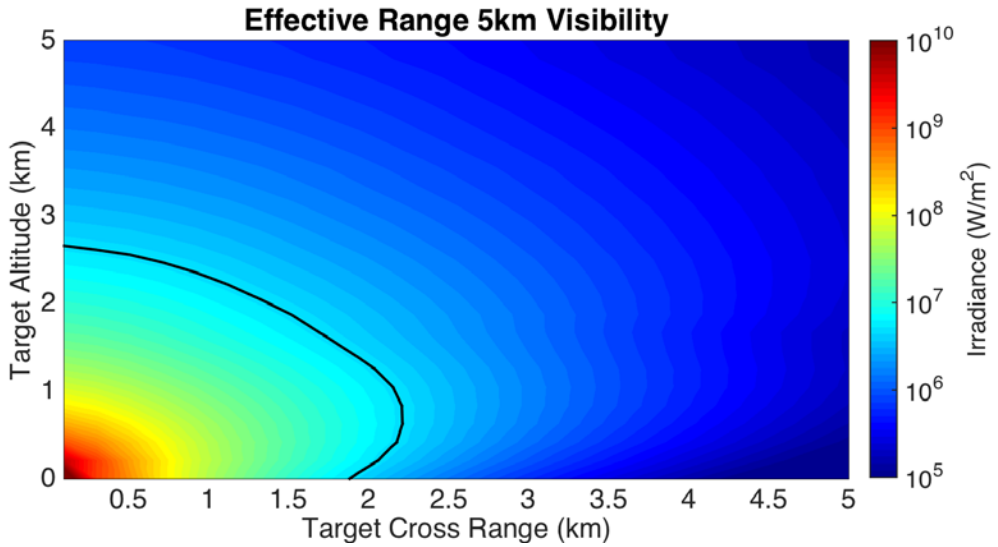

Figure 21. The effective range of a 1.0642 μm laser and 5 km of surface visibility. The relative humidity at the surface is 50 percent.

Though 1.0642 μm was not particularly sensitive to humidity, it is clearly affected by surface visibility.

Figures 22 through 25 show the effective ranges of a 1.5314 μm laser with varying surface visibility and a constant 50 percent relative humidity at the surface.

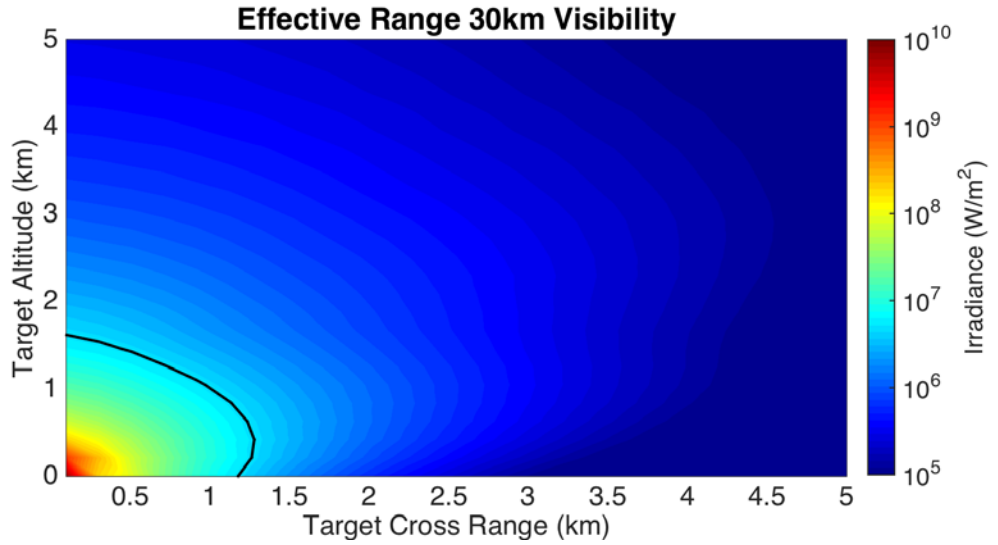

Figure 22. The effective range of a 1.5314 μm laser and 30 km of surface visibility. The relative humidity at the surface is 50 percent.

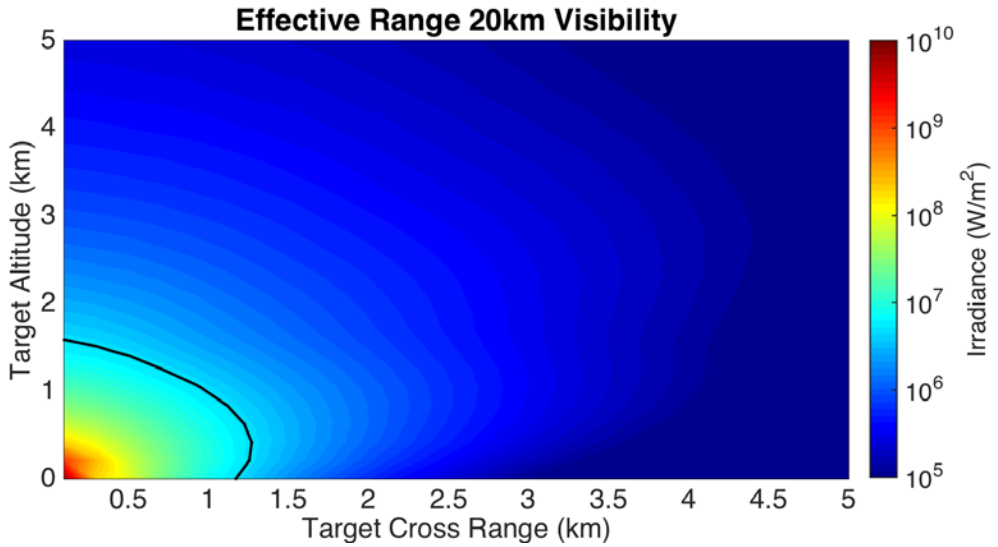

Figure 23. The effective range of a 1.5314 μm laser and 20 km of surface visibility. The relative humidity at the surface is 50 percent.

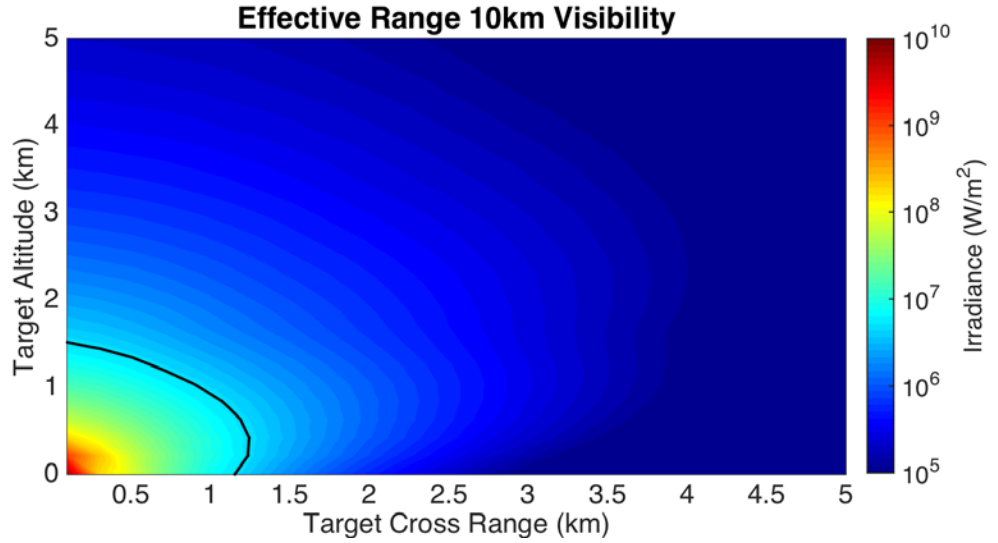

Figure 24. The effective range of a 1.5314 μm laser and 10 km of surface visibility. The relative humidity at the surface is 50 percent.

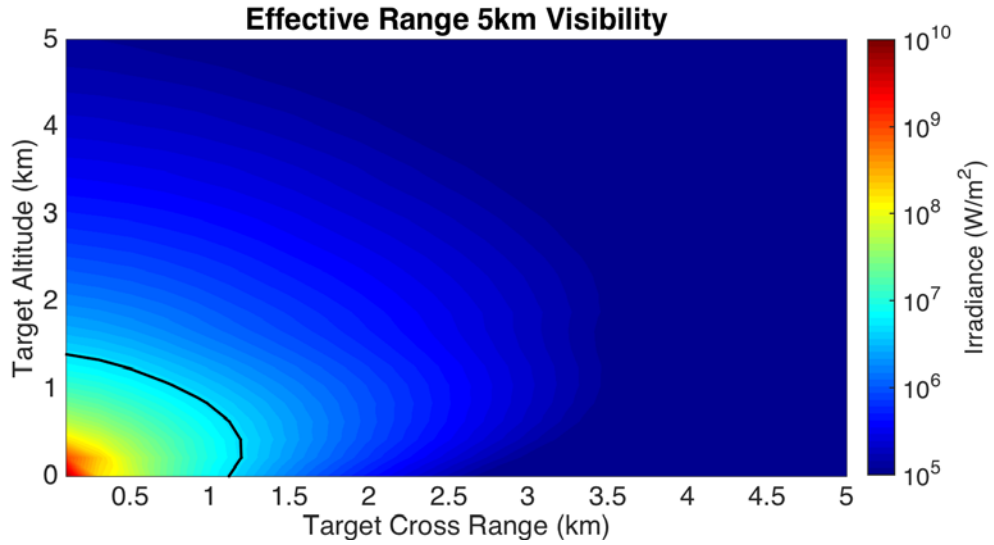

Figure 25. The effective range of a 1.5314 μm laser and 5 km of surface visibility. The relative humidity at the surface is 50 percent.

In the case of 1.5314 μm, there is very little effect on effective range from decreased visibility. As these figures illustrate, certain wavelengths can be more sensitive to visibility, which primarily influenced by aerosol scattering. In the case of 1.5314 μm there was less of an effect from hazier conditions. For 1.0642 μm however, the effective range was almost half of the value at 5 km of surface visibility relative to 30 km surface visibility.

V. EXPERIMENTAL SETUP

This experiment will measure the extinction coefficient ϵ at certain wavelengths by measuring the transmitted spectrum from a broadband source through a distance z of air. The transmission spectrum is obtained by first taking a reference spectrum of the source when the light propagates through a non-absorbing region, and then comparing this reference spectrum to one obtained when the light propagates through the sample (in this case, humid air). The sample spectrum will be attenuated relative to the reference spectrum according to Beer's law, so the fractional transmission T at a given wavelength λ is:

$$T = e^{-\epsilon(\lambda)z}. \tag{11}$$

Extinction coefficients in the atmosphere tend to be small, so long propagation distances are needed to measure appreciable attenuation. Achieving a large propagation distance in a table-top experiment requires a technique called multi-pass spectroscopy. This involves bouncing light many times between a set of mirrors [28]. The particular setup for this experiment uses a configuration of mirrors known as a White cell (WC).

Figure 26 shows a panoramic view of the entire setup. The long tube is the WC chamber; the equipment to the left of the tube consists of the light source and detector, and the equipment visible to the right of the tube is the vacuum pump.

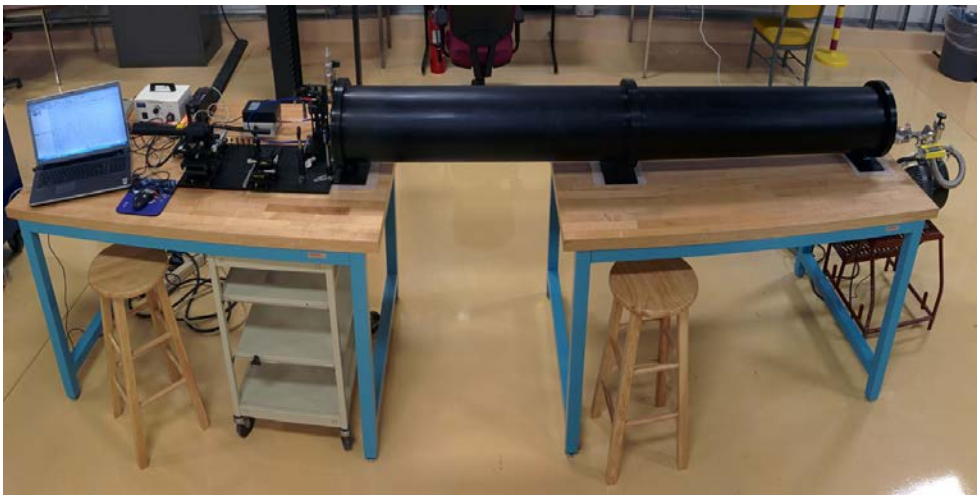

Figure 26. A panoramic view of entire experimental setup.

A. WHITE CELL

The concept of a WC was first introduced by John U. White in 1942 [29]. WCs are generally composed of two small concave mirrors and one larger concave mirror. The two small mirrors are placed opposite of the larger mirror in such a way that light enters the cell and reflects between them before exiting the cell. The number of reflections, and thus the path length, can be adjusted by realignment of the mirrors. In order to calibrate to a desired path length, an alignment laser is usually used to create well-defined dots on the larger mirror that are easy to count; the number of bounces inside the WC can then be deduced from the number of spots [29]. Figure 27 illustrates the location of the mirrors and the path that the light would take.

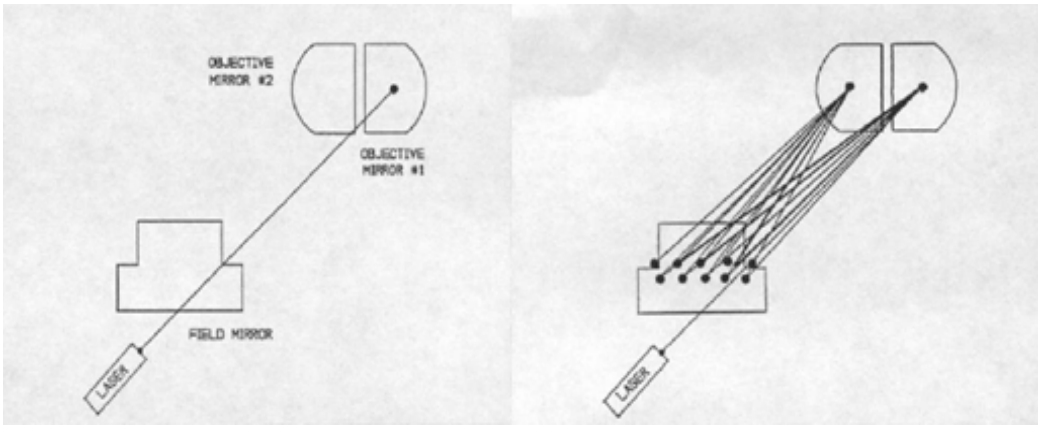

Figure 27. The three mirrors are labelled and the physical path that the light would follow has been traced. From [30], [31].

B. EXPERIMENTAL CONFIGURATION

The major components of this experiment are the source, the WC chamber, and detector. In order to maximize signal, alignment of these components is essential. Figure 28 features a diagram of these major components.

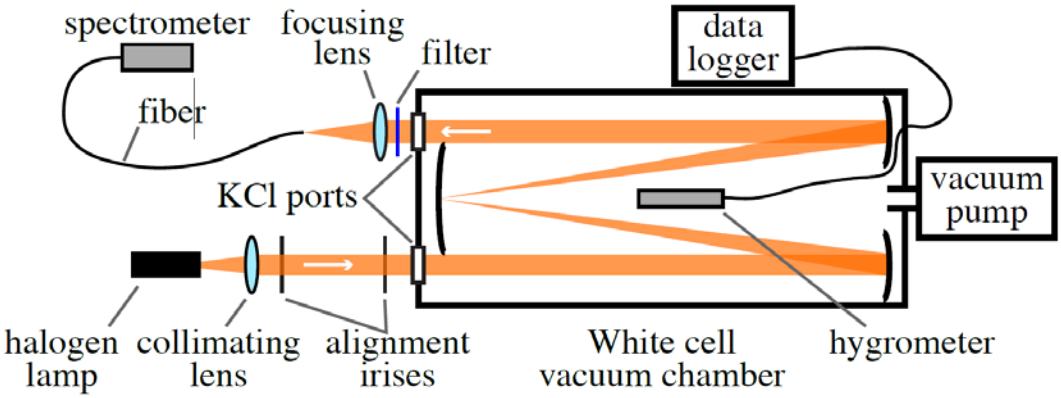

Figure 28. Major experimental components.

1. Source

Once the WC has been aligned and configured with a helium-neon (HeNe) laser, a 250 Watt quartz halogen lamp is placed in front of and aligned with the HeNe laser. The broad spectrum light leaving the halogen lamp is passed through a collimator to limit beam divergence before traveling through two irises. The irises, aligned with the HeNe beam, are used to ensure that the incident light from the lamp enters the WC chamber at a 90 degree angle with respect to the window and travels along the same path as the HeNe beam. The output of the lamp is mounted on a two-dimensional translation stage as well as a two-dimensional tilt platform to facilitate alignment.

Figure 29 shows this setup, highlighting the trajectory of the light with a yellow line. It is important to allow time for the halogen lamp's output to stabilize so as not to impart any systematic error to the transmission spectra; this process normally takes about fifteen minutes once the lamp is turned on.

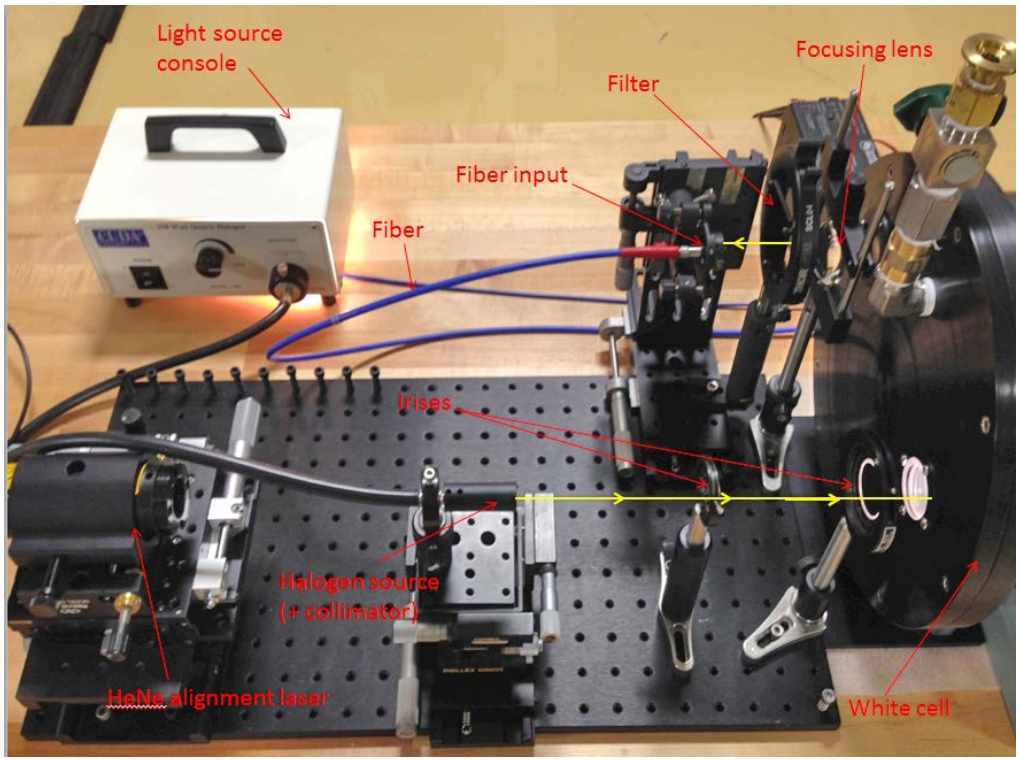

Figure 29. The experimental setup. Note the yellow line that is used to represent the trajectory of the light.

2. White Cell Chamber

The WC for this experiment is contained within a chamber that can be evacuated, as seen on the right edge of Figure 30. The input and output windows of the chamber are comprised of potassium chloride, which is transparent in the near-infrared and infrared regions. On the side of the chamber opposite of the source is the connection to a Varian vacuum pump and a pressure sensor that are used to adjust the pressure inside the chamber. At about the midpoint of the WC is a Rotronic MP100H humidity probe and a Rotronic Pt100 temperature probe that measure relative humidity and temperature inside the WC, respectively; the hygrometer and temperature probes are coupled outside of the chamber by an electronic pass-through flange. Together, these probes make up the hygrometer unit. This hygrometer was graciously provided by the Naval Postgraduate School Meteorology Department. The pump is capable of lowering the pressure inside of the chamber to a few hundred millitorr. Figure 30 shows the components described in

addition to other features. The path length is adjusted by changing the alignment of the smaller mirrors using screws accessed via ports shown in Figure 30.

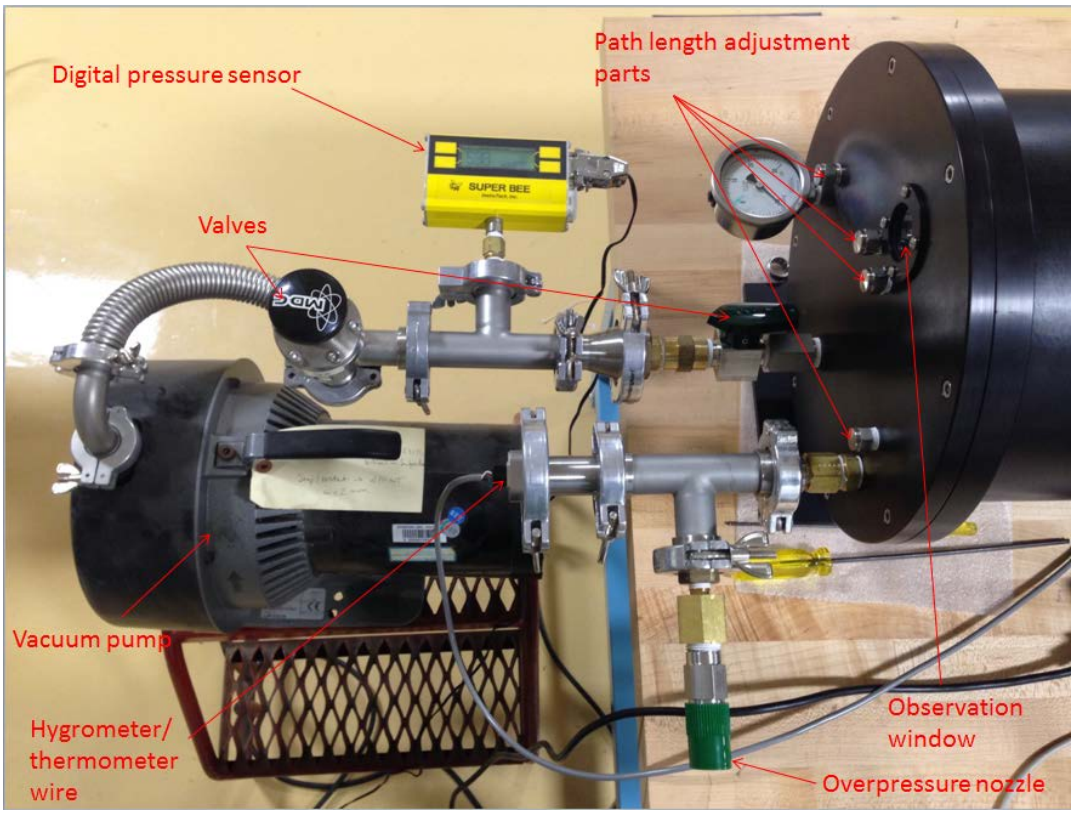

Figure 30. The side of the WC chamber opposite of the source. Various components including the roughing (vacuum) pump, hygrometer/thermometer cable, and digital pressure sensor.

The cell itself is 2.0 meters long from mirror to mirror and can be configured up to 240 meters of propagation in steps of 8.0 m. All three mirrors are coated with protected silver that is highly reflective (>96%) in the near infrared region. Figure 31 shows these three mirrors.

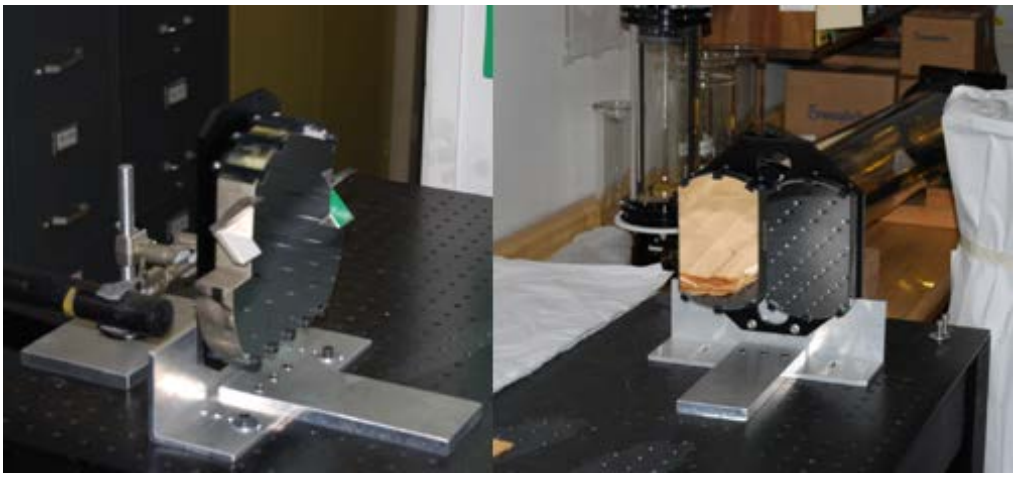

Figure 31. The three mirrors used inside of the WC to propagate light through a desired path length up to 240 meters.

The WC is configured so that the path length is proportional to the number of HeNe alignment laser dots, which can be viewed from the observation window shown in Figure 30. There are two possible configurations—one with two-rows and the other with six-rows. The latter configuration allows for longer path lengths. The general equation for the path length *l* inside of a WC is:

$$l = (\#\ of\ dots\ in\ bottom\ row)(\#\ of\ rows)(\#\ of\ passes\ per\ dot)(WC\ length). \quad (12)$$

Plugging in some known parameters for our WC, the equation simplifies to:

$$l = (\#\ of\ dots\ in\ bottom\ row)(\#\ of\ rows)(2)(2.0\ m) \quad (13)$$

Figure 32 depicts an example dot orientation using the two-row configuration while Figure 33 does the same for the six-row configuration. The number in each square represents the amount of times the light ray has traveled the length of the WC up until that point.

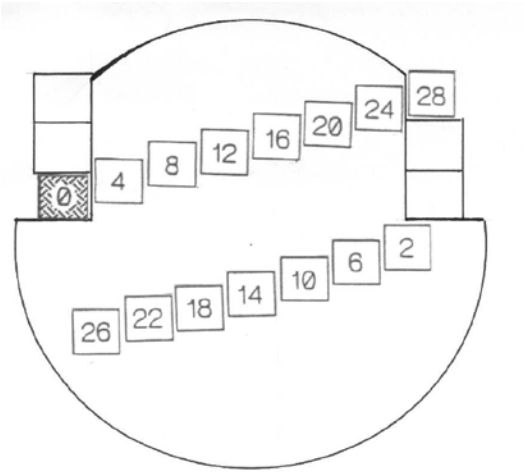

Figure 32. Sample dot orientation for the two-row configuration. The numbers represent the amount of times the light ray has traveled the length of the WC up until that point. From [31].

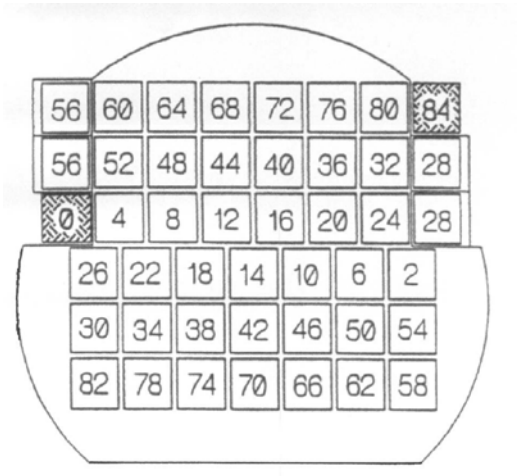

Figure 33. Sample dot orientation for the six-row configuration. The numbers represent the amount of times the light ray has traveled the length of the WC up until that point. From [31].

3. Detector

After the light has bounced off of the mirrors inside of the WC and exited the chamber, it reaches a focusing lens which denotes the beginning of the detection portion of the setup. The Ocean Optics QP1000 optical fiber that is transparent in the visible to near-infrared spectral region is placed at the focal point of the plano-convex focusing lens with a focal length of 5.0 cm. This two-meter-long fiber directs the light to an Ocean

Optics Near-Infrared-512 spectrometer, which communicates the measured spectrum to a computer running the SpectraSuite software package. This spectrometer disperses the light by a grating onto a linear array of 512 photosensitive bins. The detection range of the spectrometer is 900 nm to 1700 nm with a stated approximate 4 nm spectral resolution (though in practice we found the resolution to be much broader). A Newport FSQ-RG1000 filter is placed between the focusing lens and the fiber to remove light with a wavelength less than 1.0 μm to reduce higher order diffraction effects inside of the spectrometer. For light incident with angle θ_i on a diffraction grating, the angles of the diffracted maxima θ_m are given by

$$\theta_m = sin^{-1}\left(\frac{m\lambda}{d} - sin\,\theta_i\right), \tag{14}$$

where d is the space between each slit in the diffraction grating, integer m is the diffraction order, and λ is the wavelength of light [32]. This equation allows for several combinations of m and λ that satisfy the equation for θ_m; the filter eliminates the contributions from these subharmonics.

C. EXPERIMENTAL PROCEDURE

The simplest method for obtaining a transmission spectrum is to first take a reference spectrum when the WC chamber has been evacuated, and then measure the spectrum again when the chamber has been filled with air. As mentioned before, it is critical that this is done after providing the lamp ample time to reach a steady output state. After several trials, we noticed that the baseline for the transmission plot using this procedure was greater than one hundred percent transmission. That is, certain wavelength ranges were reporting higher transmission in one atmosphere of air than under vacuum. Figure 34 shows the measured transmission in blue and the estimated baseline of the spectrum recorded using the above process.

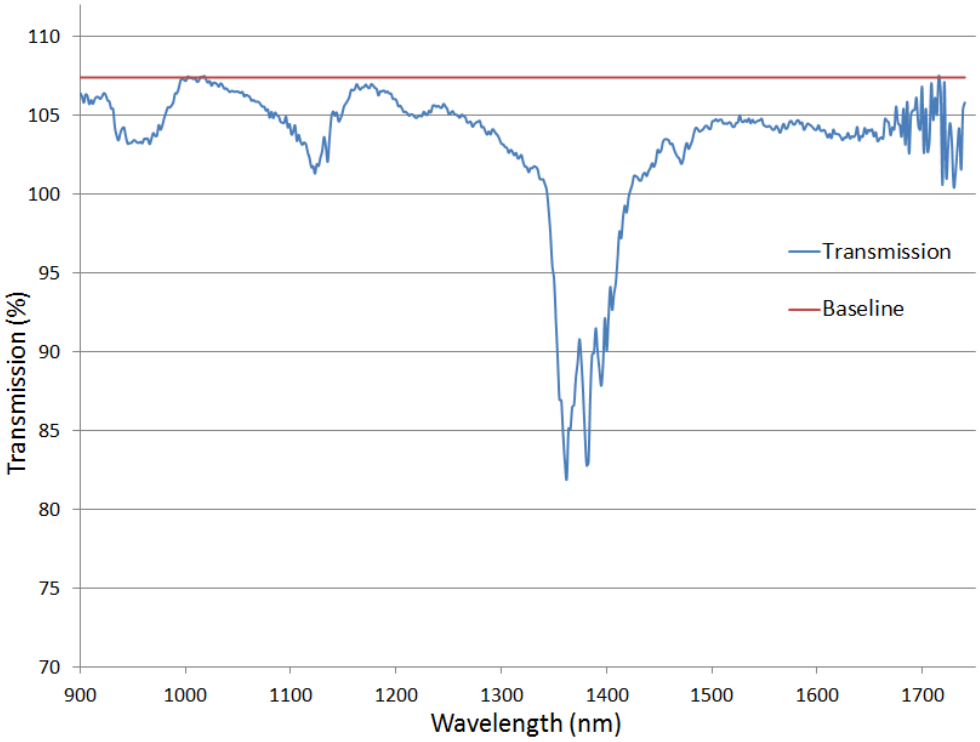

Figure 34. The baseline for the transmission spectrum is above 100 percent. The measured transmission is in blue and the estimated baseline of the spectrum is in red.

Taking this for face value would indicate that there is less attenuation in standard air than at near vacuum, which cannot be the case. This experimental artifact could be due to the many tons of force being applied to the WC when the system is under vacuum, thereby changing the alignment of the internal optical components slightly. When obtaining a transmission measurement, any changes in the signal relative to the reference spectrum should be due solely to the sample absorption; any differences due to alignment changes will produce erroneous measurements. When the situation was described to the manufacturer of the WC, Infrared Analysis Inc., they agreed that this could very well be the case. To illustrate, the total surface area of the WC is about 1.6 m^2. When the system is evacuated, the pressure difference between the outside and inside of the WC is 760 torr, and so the net force exerted on the chamber is 160 kN. This is equivalent to the weight of almost eleven average-sized cars with masses of 1400 kg each.

In order to correct for this effect, we obtained the reference spectrum while the WC chamber was filled with 760 torr of diatomic nitrogen. Nitrogen is good for these reference measurements because it has essentially no absorption in the 1 μm to 2 μm wavelength region (see Chapter III, Section A1) [19]. Using this method ensures that the reference and sample spectra are both taken when the WC is unstressed.

Before testing this method, we measured humidity in the nitrogen tank by filling the WC with nitrogen and reading the hygrometer output inside the WC. Since humidity is primarily responsible for absorption, this was to ensure that the nitrogen tank had little water content and to confirm that it would serve as a valid background measurement. Measurements showed that the relative humidity of the nitrogen at ~20°C was below 0.5 percent, well within hygrometer error of ±2 percent. We then took the reference spectrum, pumped the WC down to <300 millitorr, and let air into the chamber until the pressure reached ~760 torr, or atmospheric pressure. The result is shown in Figure 35. This method fixed the problem of transmission being reported above 100 percent.

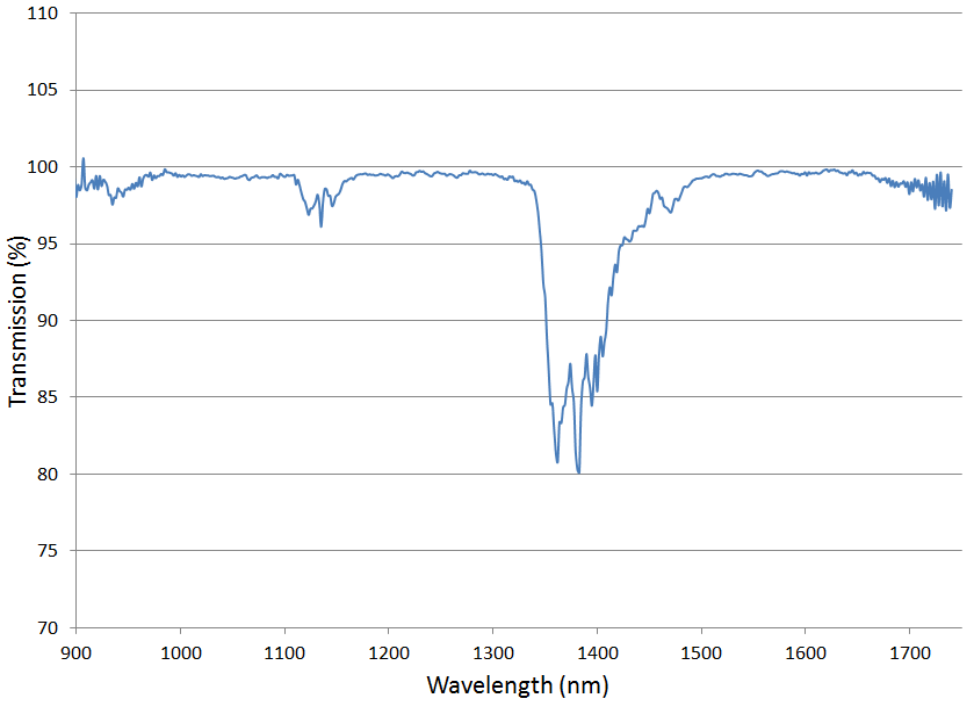

Figure 35. Transmission spectrum (after purging with nitrogen) under 100 percent as expected.

VI. RESULTS

As discussed in Section C of Chapter V, the results for this experiment were taken by first purging the White Cell (WC) with diatomic nitrogen – that is, the WC was brought to ~300 millitorr and then filled with nitrogen up to 760 torr. This process was repeated three times to ensure minimal residual humidity was left inside of the WC before taking a reference spectrum. Then, the WC was evacuated again and air was allowed to fill the WC as the transmission spectrum and climate parameters (relative humidity and temperature inside the WC) were documented as functions of time.

One might notice that in this chapter there is little distinction made between absorption and extinction. This is because in the wavelength range that we see the most attenuation (1300 nm to 1400 nm), the molecular absorption coefficient is several orders of magnitude larger than the other three that make up the total extinction coefficient [15]. Therefore, the absorption and total extinction are nearly the same in this wavelength range.

A. INITIAL RESULTS

The WC was configured and spectra were taken for three path lengths: 24 m, 40 m, and 64 m. Figure 36 shows the transmission spectra for these path lengths. Certain wavelengths are labeled and will be discussed further later in this section.

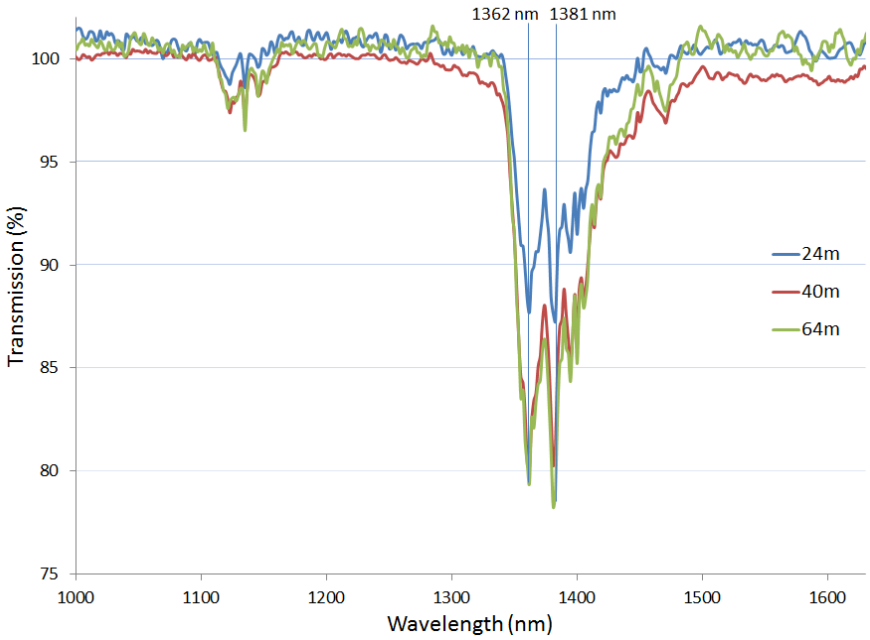

Figure 36. Transmission spectra for three path lengths: 24 m, 40 m, and 64 m.

The corresponding humidity and temperature recorded for each curve in Figure 36 are listed in Table 3.

Path Length (m)	Relative Humidity (%)	Temperature (K)
24	6.8	293.2
40	6.5	293.7
64	5.2	292.0

Table 3. Humidity and temperature values for their corresponding path lengths.

As explained in further detail in Section IV of this chapter, there is evidence that questions the accuracy of the humidity measurements made by the hygrometer. This makes it tricky to simulate plots on LEEDR that can be compared to our experimental data. However, we can use Beer's Law to calculate the extinction coefficient for the three path lengths at various wavelengths as a first step in our analysis:

$$\epsilon = -\frac{ln\,T}{z}, \tag{15}$$

where T is the fractional transmission and z is the path length [13].

The extinction coefficient was calculated at two points on the transmission spectrum which are labeled on Figure 36. The calculated values are shown in Table 4.

Wavelength (nm)	**ϵ for 24m (km^{-1})**	**ϵ for 40m (km^{-1})**	**ϵ for 64m (km^{-1})**
1362	5.5	5.5	3.6
1381	5.5	5.5	3.8

Table 4. Calculated extinction coefficients for two wavelengths and each path length in Figure 36.

As a sanity check, it is nice to see that the measured extinction coefficients for these two examples are relatively close to one another. Preliminarily, we can presume that the differences in the 64 m outlier can be attributed to the differences in humidity compared to the other two path lengths. However, to really determine whether the data is self-consistent, we need to dig deeper by calculating the corresponding extinction cross sections for each data set.

To convert from relative humidity *RH* to absolute humidity *AH,* we can start with the relationship in equation (16):

$$AH = \frac{M_w e}{RT}, \tag{16}$$

where T is the temperature in Kelvin, R is the molar gas constant (8.31 J/mol K), M_w is the molar mass of water (18 g/mol)[33]. In equation (17), e is the vapor pressure which is related to the relative humidity in the following way:

$$e = \frac{RH \times e_s}{100}. \quad (17)$$

In equation (17), *RH* is measured as a percent and e_s is the vapor pressure at saturation, which is dependent on the temperature and pressure of the system [33]. A good approximation for the saturation vapor pressure at an atmospheric pressure of 760 torr is given by the Tetens equation [33]:

$$e_s(T) = (.611\ kPa) exp[\frac{17.27(T - 273\ K)}{T - 36\ K}]. \quad (18)$$

This leaves us with the tools necessary to calculate the absolute humidity with just the relative humidity and temperature.

Finding the absolute humidity using the previous equations produces an answer with units of grams per unit volume; which can then be converted the particle density *N*:

$$N = AH \times \frac{1\ mole\ of\ water}{18.015g} \times \frac{6.022 \times 10^{23} particles}{1\ mole\ of\ water}. \quad (19)$$

The absolute humidity and particle density values for the three path lengths mentioned are shown in Table 5:

Path length (m)	Absolute Humidity (g/m^3)	N ($1x10^{22}$ particles/m^3)
24	1.2	3.9
40	1.2	3.9
64	.85	2.8

Table 5. Absolute humidity and N values for their corresponding path lengths.

Using equation (2) from Chapter III, Section A, and assuming that the absorption coefficient is approximately equal to the extinction coefficient, we can solve for the absorption cross section σ, which is related to the probability that a single water molecule will absorb a photon and is (approximately) independent of the relative humidity [21]:

$$\sigma = \frac{\alpha_m}{N} \cong \frac{\epsilon_{tot}}{N}. \quad (20)$$

The cross sections for both wavelengths mentioned in Table 4 can be found on Table 6.

Path length (m)	σ (kb), λ=1362nm	σ (kb), λ=1381nm
24	1.4	1.4
40	1.4	1.4
64	1.3	1.4

Table 6. Cross sections σ, for their corresponding path lengths and two chosen wavelengths. The cross section is related to the probability that a single water molecule will absorb a photon and temperature values for their corresponding path lengths. Note that the units for the cross sections are in kilobarns (10^{-25} m^2).

As can be seen, the measured cross section values at each wavelength are relatively close to one another. This close proximity for σ shows that the data is self-consistent. Comparison to theoretical values requires determination of detector resolution and hygrometer accuracy.

B. DETECTOR RESOLUTION AND CALIBRATION

A common method for calculating the resolution of a spectrometer involves determining $S_r(\lambda)$ and $R(\lambda)$, the linewidth of the signal and spectral resolution of the spectrometer, respectively. The observed signal is then equal to the convolution of the two, as shown in equation (21) [34].

$$S_o(\lambda) = S_r(\lambda) * R(\lambda) \tag{21}$$

Ideally, the resolution of a detector can be found using atomic emission sources. This is because an atomic emission line is significantly usually much narrower, with a width on the order of 10^{-4} angstroms, than the detector's spectral resolution [34]. If so, then, according to the above equation, the measured line width reduces to the detector resolution for such narrow spectral sources. However, after analyzing the spectrums of xenon, krypton, and mercury, none were found to emit brightly enough to be detected in the 1.4 μm to 1.6 μm window where we observed maximum absorption.

As an alternative, a CO_2 spectrum was taken by first purging the WC with nitrogen, bringing it down to ~300 millitorr, and then filling it with CO_2 to a pressure of

760 torr. This provided an experimental CO_2 absorption spectrum that could be compared to the known CO_2 spectrum. These two spectra are shown on Figure 37; the theoretical plot is taken from the HITRAN Molecular Absorption Database [19]. The HITRAN plot is shown in green and the experimental plot in blue:

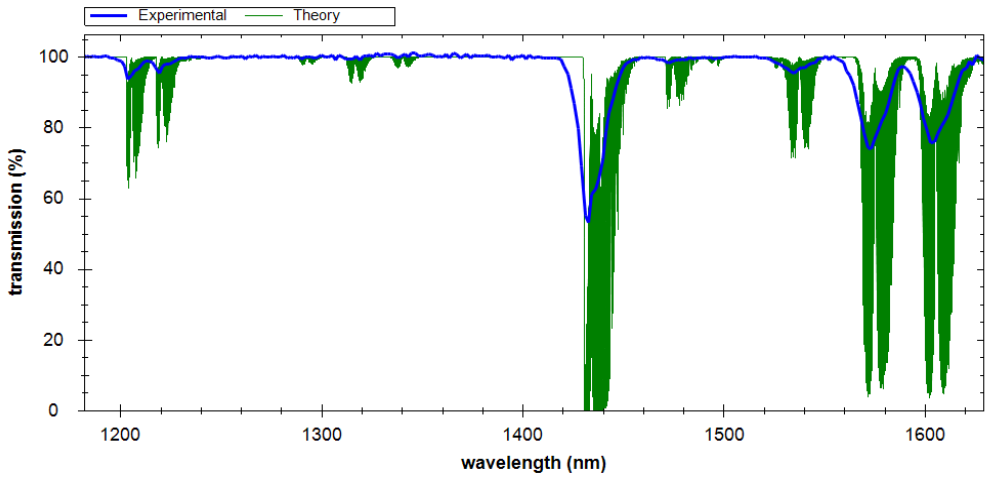

Figure 37. Experimental spectra and the HITRAN simulated spectra for CO_2. The HITRAN plot is shown in green and the experimental plot in blue. After [19].

There are two noticeable differences between the measured spectrum and the HITRAN spectrum. First, the measured spectrum has a much lower resolution. The Ocean Optics spectrometer used in this study has a stated resolution of about 4.0 nm; clearly, the measured spectrum does not display this level of fidelity. Second, the measured spectrum is slightly shifted to shorter wavelengths compared with HITRAN, likely due to a slight offset of the spectrometer's reading.

We can obtain a rough estimate of the detector response by applying a moving average (with a similar short wavelength bias) to the HITRAN data. This "smoothed" curved is shown in red in Figure 38.The red curve, which fits the experimental data fairly well, was produced by setting the width of the moving average window to 30 nm and biasing the window with a 12 nm offset toward shorter wavelengths.

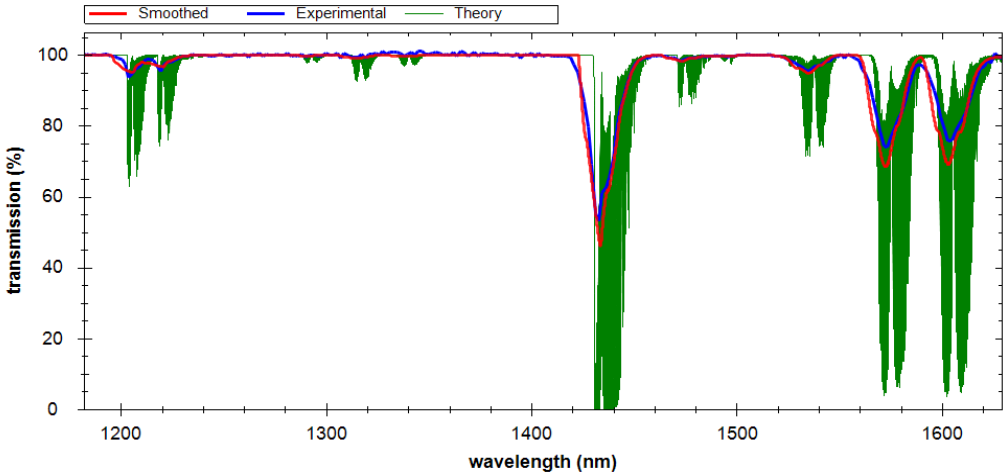

Figure 38. Experimental spectra, the HITRAN simulated spectra, and a smoothed HITRAN spectra for CO_2. The smoothed plot was used to estimate the detector resolution. The HITRAN plot is shown in green, the experimental plot in blue, and the smoothed plot in red. After [19].

More complex convolution/deconvolution methods could better characterize the detector response [35]. However, those methods could not be explored for this thesis due to time constraints.

C. COMPARISON TO LEEDR

With a rough estimate for our spectrometer resolution and the humidity and temperature measured by our hygrometer, we can compare our data to simulated LEEDR data. Figures 39 through 41 show the LEEDR data in green, our experimental data in blue, and the smoothed LEEDR data in red for 24 m, 40 m, and 64 m path lengths, respectively. Just as for the CO_2 spectrum, the LEEDR data was averaged to account for a 30 nm detector resolution and biased by 12 nm to shorter wavelengths.

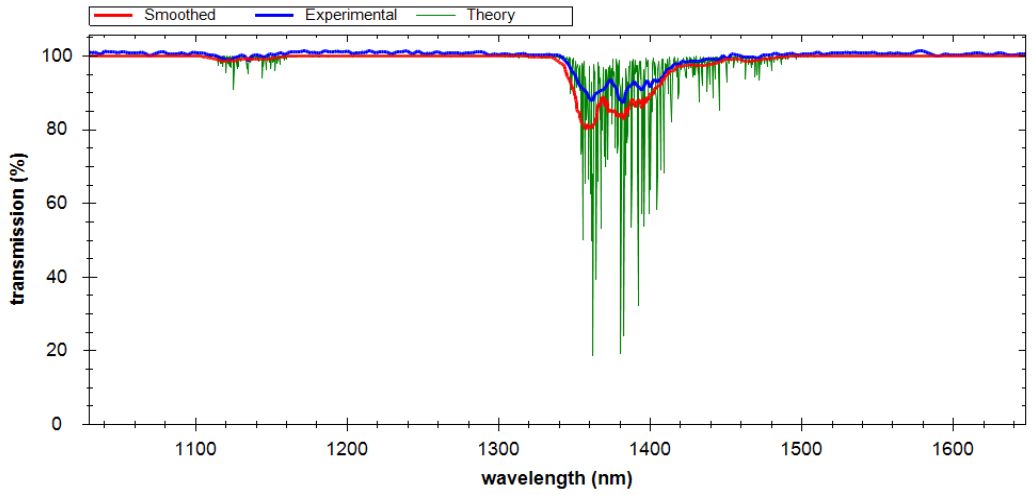

Figure 39. Experimental spectra (blue), the LEEDR simulated spectra (green), and a smoothed LEEDR plot (red) for the atmospheric absorption in 24 m of air. After [15].

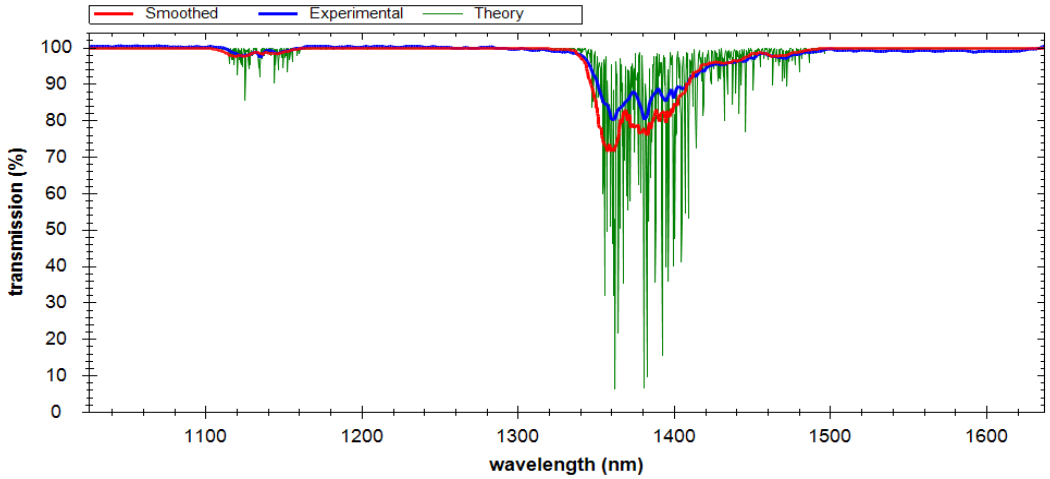

Figure 40. Experimental spectra (blue), the LEEDR simulated spectra (green), and a smoothed LEEDR plot (red) for the atmospheric absorption in 40 m of air. After [15].

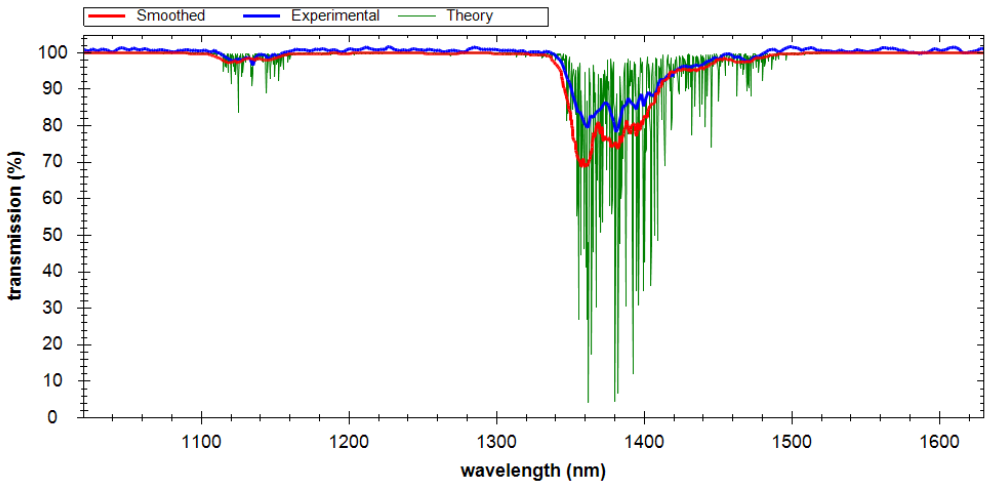

Figure 41. Experimental spectra (blue), the LEEDR simulated spectra (green), and a smoothed LEEDR plot (red) for the atmospheric absorption in 64 m of air. After [15].

On all three plots, we can see the benefit of the CO_2 calibration when we compare the red and green curves to the blue. On these plots, the red and blue curves seem to have the same shape and seem to differ mostly in depth. This difference is most likely due to characteristics related to the detector and the uncertainty in the humidity measurements. In order to be able to take this analysis further, a higher resolution spectrometer is recommended.

D. MEASURING HUMIDITY

We know that the extinction coefficient is closely related to humidity through molecular absorption. As mentioned in the introduction to this chapter, we know that the molecular absorption is the prevailing coefficient out of the four that make up the extinction coefficient [15]. Therefore, we expect that our transmission spectrum will be closely related to the humidity measured in the WC. Figure 42 shows several transmission spectra for the 40 m path length taken over the course of about an hour with corresponding humidity measurements as reported by the hygrometer.

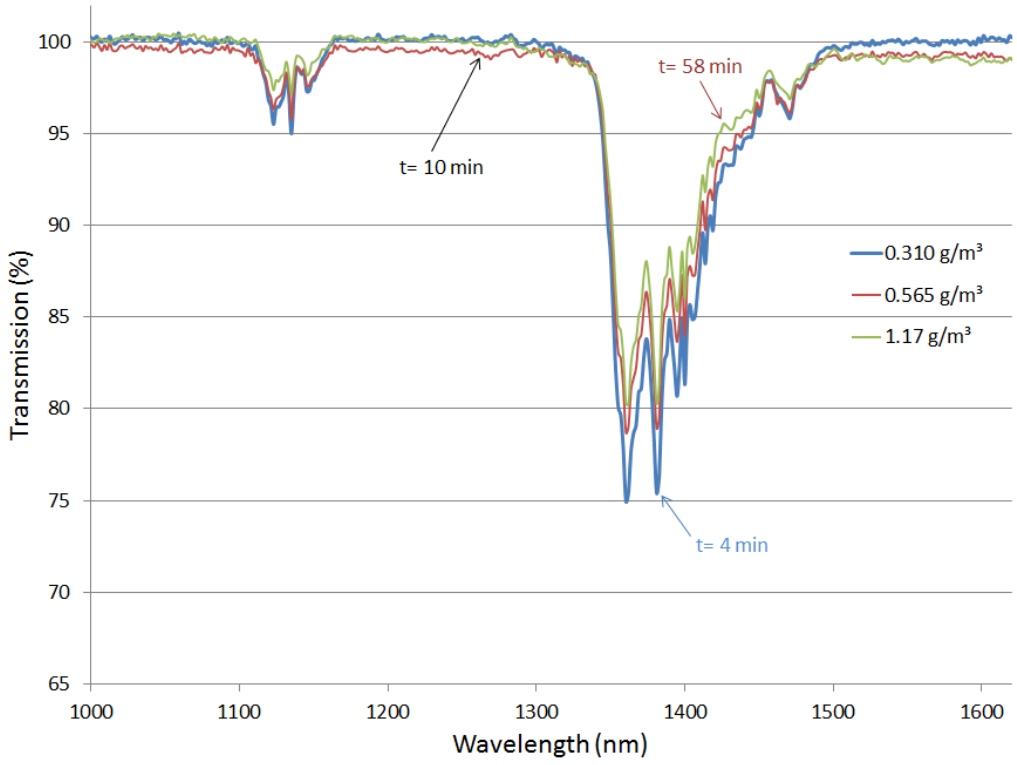

Figure 42. Several transmission spectra for a 40 m path length taken over the course of about an hour with corresponding humidity measurements as reported by the hygrometer. The timestamps correspond to $t = 0$ being when air was allowed to flow into the WC.

The times labeled in Figure 42 indicated when the spectrum was taken relative to the when air was let into the WC. The absolute humidity (calculated from the hygrometer data) as a function of time is plotted on Figure 43. The time domain (the x-axis) begins with negative values to show that the WC was at a steady state until $t = 0$ when air is let into the WC. The points at which the plots in Figure 42 were taken are denoted with dots in Figure 43.

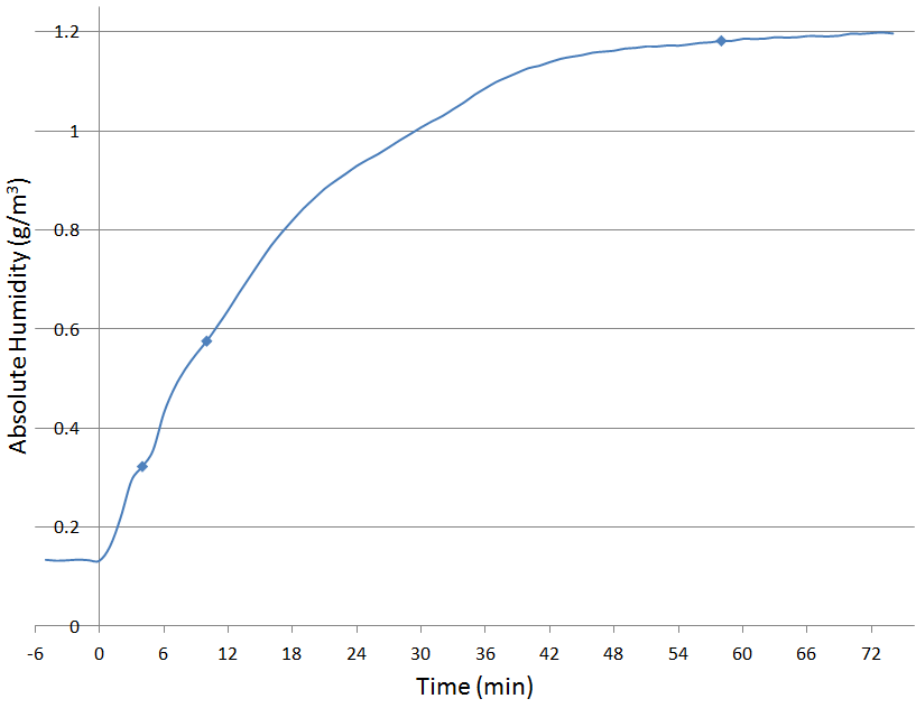

Figure 43. Humidity (as reported by the hygrometer) as a function of time. The time domain (the x-axis) begins with negative values to show that the WC was at a steady state until $t = 0$ when air is let into the WC. The points at which the plots in Figure 42 were taken are denoted with dots.

As can be noted by comparing Figure 42, absorption seems to be decreasing with time while the humidity is increasing. This cannot be correct since humidity is the prime contributor of atmospheric extinction. Additionally, the transmission spectra in Figure 42 do not change as much as LEEDR would predict if the hygrometer data were correct. As shown by Figure 44, which depicts plots generated using LEEDR data, we expect there to be an approximate direct proportionality between absolute humidity and absorption rather than the inverse one suggested by the experimental data.

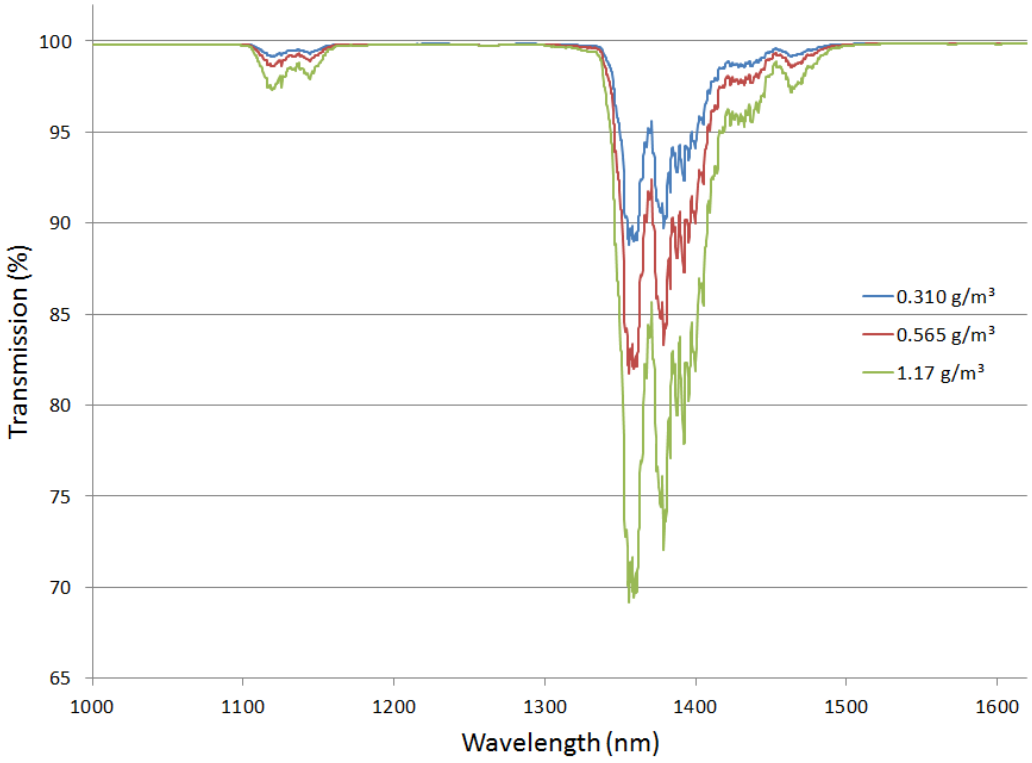

Figure 44. Plot of transmission vs. wavelength using LEEDR-supplied data for a 40 m path length, for several values of absolute humidity. After [15].

The conclusion is that the hygrometer measurement is inconsistent with the observed spectra. This is likely due to a systematic error in the hygrometer reading. Cycling the hygrometer through vacuum might have affected its sensitivity in some way, and most hygrometers have limited accuracy below a relative humidity of ~2%. This makes it difficult to compare the observed spectra with the ones predicted by LEEDR without knowing what the relative humidity really is. Moving forward with this experiment, a vacuum-certified hygrometer is recommended and one that is more sensitive to smaller values of the relative humidity.

E. FUTURE RECOMMENDATIONS AND SUMMARY

In order to circumvent the aforementioned detector resolution issue, a higher resolution, more sensitive detector is recommended going forward with this experiment. There is a Fourier Transform Infrared Detector (FTIR) available that would be a considerable upgrade once a near-infrared source is purchased and installed in it.

Previous results taken in the 2.5 μm to 12 μm wavelength window with an FTIR over a path length of 10 m are shown in the Figure 45; also shown is a plot generated by LEEDR [15]. The FTIR spectrum is highly detailed and matches the trends predicted by LEEDR very well. Undoubtedly, we can see much more definition in the plot generated from FTIR data than in the plot generated by our Ocean Optics Near-Infrared-512 spectrometer.

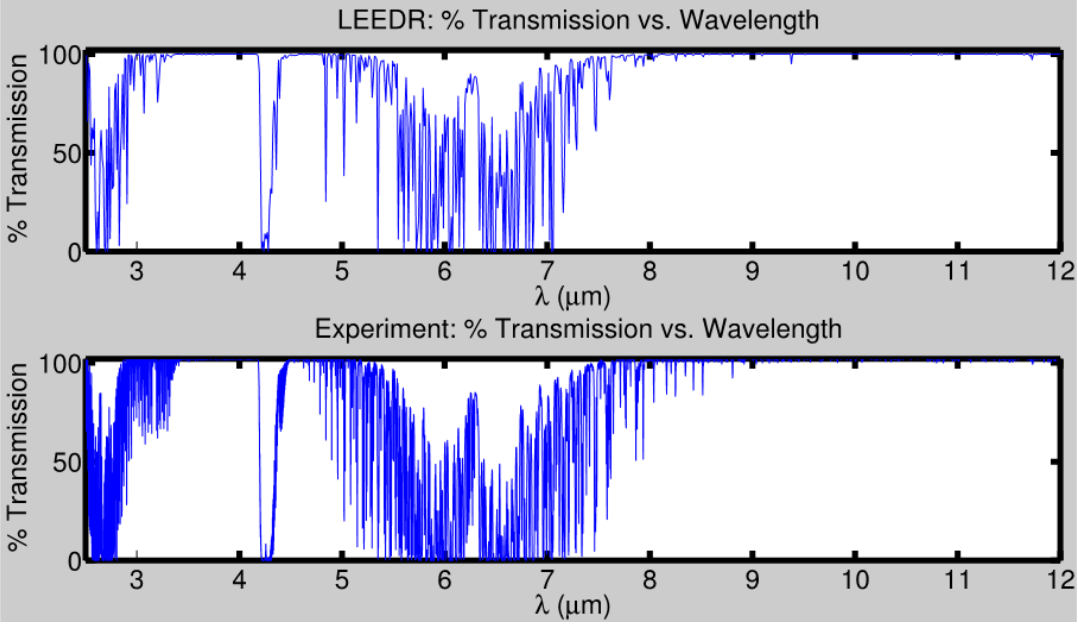

Figure 45. Results that were taken in the 2.5 μm to 12 μm wavelength window with an FTIR over a path length of 10 m. Note the high resolution of the FTIR detector. From [15].

As mentioned before, another improvement would be to use a better hygrometer – that is, one that works when cycled through a vacuum and is accurate at lower relative humidity levels. As mentioned in Section IV of this chapter, we are unsure about the effects that low pressures can have on the hygrometer sensor. What is clear is that there seemed to be little, if any, correlation between the spectra obtained while the hygrometer readings were undergoing transients. However, once the hygrometer measurements had stabilized, the calculated absorption cross sections were consistent between measurements, though a bit smaller than what LEEDR would predict for a given relative humidity, temperature, and estimated detector resolution.

THIS PAGE INTENTIONALLY LEFT BLANK

VII. CONCLUSION

This research looked at atmospheric effects on laser propagation by employing both simulation and experimental methods.

A. SIMULATION

The simulation portion used ANCHOR and LEEDR to evaluate the performance of two 100kW lasers, one operating at a wavelength of 1.0642 μm, and the other at a wavelength of 1.5314 μm in a potential operating theater. The laser operating at 1.0642 μm proved to be greatly affected by increased haze, but not humidity. When surface visibility was reduced from 30 km to 5 km and relative humidity was held constant at 50 percent, the effective range at most target altitudes was nearly halved. Conversely, the laser operating at 1.5314 μm demonstrated a large dependence on humidity, but not haze. When relative humidity was raised from 10 to 90 percent and surface visibility was held constant at 30 km, the effective range at most target altitudes was nearly halved. This modeling illustrated that the effective range of the laser can be greatly dependent on aerosol scattering (haze), molecular absorption (humidity), or both, depending on its lasing wavelength.

B. EXPERIMENT

The experimental portion involved employing a multipath WC chamber that can be used to measure extinction coefficients. The initial results from three different path lengths (24 m, 40 m, and 64 m) indicate that the chamber is suitable to consistently measure absorption features based upon the calculated absorption cross sections obtained from the experimental data at the three path lengths. Additionally, the observance of contradictory patterns related to humidity measurements and absorption suggested uncertainty of the measurements produced by the hygrometer. In order to achieve more precise measurements, upgrades to the hygrometer and detector are required.

THIS PAGE INTENTIONALLY LEFT BLANK

LIST OF REFERENCES

[1] R. O'Rourke, "Navy shipboard lasers for surface, air, and missile defense: Background and issues for Congress," Congressional Research Service Report R41526, Jun. 2013.

[2] P. A. Morrison and S. Niles. (2012, Sept.). *Solid state laser maturation program* [Online]. Available: http://www.onr.navy.mil/~/media/Files/Fact-Sheets/35/Solid-State-Laser-Technology-Maturation-Program-2012-a.ashx.

[3] Q. Saulter. (2014). *High-energy laser* [Online]. Available: http://www.onr.navy.mil/Media-Center/Fact-Sheets/High-Energy-Laser.aspx.

[4] G. P. Perram et al., *Introduction to Laser Weapon Systems,* 1st ed. Albuquerque, NM: Directed Energy Professional Society, 2010.

[5] K. Erickson. (2015, May). What is a laser? [Online]. Available http://spaceplace.nasa.gov/laser/en/

[6] National Ignition Facility and Photon Science. (2010, Feb.). How do lasers work? [Online]. Available: https://lasers.llnl.gov/content/assets/docs/news/pk_how_lasers_work.pdf

[7] Office of Naval Research. (2014, Apr.) All systems go: Navy's laser weapon ready for summer deployment. [Online]. Available: http://www.navy.mil/submit/display.asp?story_id=80172.

[8] M. Alvarez, "Feasibility of high energy laser weapons onboard USMC attack helicopters," M.S. thesis, Physics Dept., Naval Postgraduate School, Monterey, CA, 2013.

[9] W. Colson. (2014, Oct.). 'Electric ship weapon systems', Monterey, Ca [Powerpoint slides].

[10] R. Kale, *PROGRAM ACQUISITION COST BY WEAPON SYSTEM*, 1st ed. Washington D.C.: Department of Defense, 2014, p. 63.

[11] K.R. Cohn. (2014, Oct.). 'High Power Solid-state Lasers', Monterey, Ca [PowerPoint slides].

[12] R. P. Mansfield, "High energy solid state and free electron laser systems in tactical aviation," M.S. thesis, Physics Dept., Naval Postgraduate School, Monterey, CA, 2005.

[13] G. Lothian, 'Beer's law and its use in analysis. A review', *Analyst*, vol. 88, no. 1050, p. 678, 1963.

[14] K. N. Liou, *An Introduction to Atmospheric Radiation*, 2nd ed. San Diego, CA: Academic Press, 2002.

[15] S. T. Fiorino. (2013). *The laser environmental effects definition and reference (LEEDR)* [Online]. Available: http://www.afit.edu/CDE/page.cfm?page=329&tabname=Tab5A.

[16] Skbkekas. (2010, Mar.). Plots of the density functions for several members of the Cauchy family of probability distributions. [Online]. Available: http://upload.wikimedia.org/wikipedia/commons/8/8c/Cauchy_pdf.svg.

[17] F. Evans. (2001, Sept.). Absorption line physics. [Online]. Available: http://nit.colorado.edu/atoc5560/week4.pdf.

[18] G. W. Petty, *A First Course in Atmospheric Radiation*, 2nd ed. Madison, WI: Sundog Publishing, 2004.

[19] L. S. Rothman et al., "The HITRAN2012 molecular spectroscopic database," *Journal of Quantitative Spectroscopy and Radiative Transfer*, vol. 130, Apr. 2013.

[20] B. E. Rocher-Casterline et al., "Communication: Determination of the bond dissociation energy of the water dimer, (H2O)2, by velocity map imaging," *J. Chem. Phys*., vol. 130, Jun. 2011.

[21] K.R. Cohn. (2014, Oct.). 'Atmospheric Extinction', Monterey, Ca [PowerPoint slides].

[22] C. Mätzler and J. Ricka. (2009). *Radiative transfer* [Online]. Available: http://www.iapmw.unibe.ch/teaching/vorlesungen/radiative_transfer/skript/Lecture2009_9.pdf.

[23] S. W. Cheong and K. L. Woon, "Modeling of light extraction efficiency of scattering thin film using Mie scattering," *Optica Applicata*, vol. XLI, no. 1, 2011.

[24] P. E. Nielsen, *Effects of Directed Energy Weapons*. Albuquerque, NM: Directed Energy Professional Society, 2009.

[25] C.R. Fussman, "High energy laser propagation in various atmospheric conditions utilizing a new accelerated scaling code," M.S. thesis, Physics Dept., Naval Postgraduate School, Monterey, CA, 2014.

[26] S. Coy. (2013). *WaveTrain: A user-friendly wave optics propagation code* [Online]. Available: https://www.mza.com/publications/wtspiepaper.htm.

[27] K.R. Cohn, J. Blau, W.B. Colson, and C. Fussman. (2014, Oct.). 'Physics-based Modeling of Atmospheric Propagation for High Energy Lasers', Monterey, Ca [PowerPoint slides].

[28] R. Curl and F. Tittel, '7 Tunable infrared laser spectroscopy', *Annual Reports Section "C" (Physical Chemistry)*, vol. 98, pp. 228-270, 2002.

[29] J.U. White, "Long optical paths of large aperture," *J. Opt. Soc. Am*. Vol. 32, pp. 285–285, 1942.

[30] P.L. Hanst. Long path gas cells. [Online]. Available: http://www.infraredanalysisinc.com/l5.htm

[31] *Variable Path length Long Path Cell*, 1st ed. Aneheim, 2012, p. 6.

[32] E. Loewen and E. Popov, *Diffraction gratings and applications*. New York: M. Dekker, 1997.

[33] P. Calow, *The encyclopedia of ecology & environmental management*. Osney Mead, Oxford: Blackwell Science, 1998.

[34] B&W Tek, 'Part 5: Spectral Resolution - B&W Tek', 2015. [Online]. Available: http://bwtek.com/spectrometer-part-5-spectral-resolution/. [Accessed: 29- May- 2015].

[35] W. Blass and G. Halsey, *Deconvolution of absorption spectra*. New York: Academic Press, 1981.

THIS PAGE INTENTIONALLY LEFT BLANK

INITIAL DISTRIBUTION LIST

1. Defense Technical Information Center
   Ft. Belvoir, Virginia

2. Dudley Knox Library
   Naval Postgraduate School
   Monterey, California